A&A 528, A120 (2011)
DOI: 10.1051/0004-6361/201015768

Astronomy & Astrophysics

Radiative hydrodynamic simulations of red supergiant stars

III. Spectro-photocentric variability, photometric variability, and consequences on Gaia measurements

A. Chiavassa[1,2], E. Pasquato[1], A. Jorissen[1], S. Sacuto[3], C. Babusiaux[4], B. Freytag[5,6,7], H.-G. Ludwig[8], P. Cruzalèbes[9], Y. Rabbia[9], A. Spang[9], and O. Chesneau[9]

[1] Institut d'Astronomie et d'Astrophysique, Université Libre de Bruxelles, CP. 226, Boulevard du Triomphe, 1050 Bruxelles, Belgium
e-mail: achiavas@ulb.ac.be
[2] Max-Planck-Institut für Astrophysik, Karl-Schwarzschild-Str. 1, Postfach 1317, 85741 Garching b. München, Germany
[3] Department of Astronomy, University of Vienna, Türkenschanzstrasse 17, 1180 Wien, Austria
[4] GEPI, Observatoire de Paris, CNRS, Université Paris Diderot, Place Jules Janssen, 92190 Meudon, France
[5] Université de Lyon, 69003 Lyon; École Normale Supérieure de Lyon, 46 allée d'Italie, 69007 Lyon; CNRS, UMR 5574, Centre de Recherche Astrophysique de Lyon; Université Lyon 1, 69622 Villeurbanne, France
[6] Department of Physics and Astronomy, Division of Astronomy and Space Physics, Uppsala University, Box 515, S-751 20 Uppsala, Sweden
[7] Istituto Nazionale di Astrofisica, Osservatorio Astronomico di Capodimonte, via Moiariello 16, 80131 Naples, Italy
[8] Zentrum für Astronomie der Universität Heidelberg, Landessternwarte, Königstuhl 12, 69117 Heidelberg, Germany
[9] UMR 6525 H. Fizeau, Univ. Nice Sophia Antipolis, CNRS, Observatoire de la Côte d'Azur, Av. Copernic, 06130 Grasse, France

Received 16 September 2010 / Accepted 17 December 2010

ABSTRACT

Context. It has been shown that convection in red supergiant stars (RSG) gives rise to large granules that cause surface inhomogeneities and shock waves in the photosphere. The resulting motion of the photocentre (on time scales ranging from months to years) could possibly have adverse effects on the parallax determination with Gaia.
Aims. We explore the impact of the granulation on the photocentric and photometric variability. We quantify these effects in order to better characterise the error that could possibly alter the parallax.
Methods. We use 3D radiative-hydrodynamics (RHD) simulations of convection with CO5BOLD and the post-processing radiative transfer code Optim3D to compute intensity maps and spectra in the Gaia *G* band [325–1030 nm].
Results. We provide astrometric and photometric predictions from 3D simulations of RSGs that are used to evaluate the possible degradation of the astrometric parameters of evolved stars derived by Gaia. We show in particular from RHD simulations that a supergiant like Betelgeuse exhibits a photocentric noise characterised by a standard deviation of the order of 0.1 AU. The number of bright giant and supergiant stars whose Gaia parallaxes will be altered by the photocentric noise ranges from a few tens to several thousands, depending on the poorly known relation between the size of the convective cells and the atmospheric pressure scale height of supergiants, and to a lower extent, on the adopted prescription for galactic extinction. In the worst situation, the degradation of the astrometric fit caused by this photocentric noise will be noticeable up to about 5 kpc for the brightest supergiants. Moreover, parallaxes of Betelgeuse-like supergiants are affected by an error of the order of a few percents. We also show that the photocentric noise, as predicted by the 3D simulation, does account for a substantial part of the supplementary "cosmic noise" that affects Hipparcos measurements of Betelgeuse and Antares.

Key words. stars: atmospheres – supergiants – astrometry – parallaxes – hydrodynamics – stars: individual: Betelgeuse

1. Introduction

The main goal of the Gaia mission (Perryman et al. 2001; Lindegren et al. 2008) is to determine high-precision astrometric parameters (i.e., positions, parallaxes, and proper motions) for one billion objects with apparent magnitudes in the range $5.6 \leq V \leq 20$. These data along with multi-band and multi-epoch photometric and spectrocopic data will allow us to reconstruct the formation history, structure, and evolution of the Galaxy. Among all the objects that will be observed, late-type stars present granulation-related variability that is considered, in this context, as "noise" that must be quantified in order to better characterise any resulting error on the parallax determination. A previous work by Ludwig (2006) has shown that effects caused by the granulation in red giant stars are unlikely to be important except for the extreme giants.

Red supergiant (RSG) stars are late-type stars with masses between 10 and 40 $M_{\odot}$. They have effective temperature $T_{\rm eff}$ ranging from 3450 (M5) to 4100 K (K1), luminosities in the range of 2000 to 300 000 $L_{\odot}$, and radii up to 1500 $R_{\odot}$ (Levesque et al. 2005). Their luminosities place them among the brightest stars, and they are visible up to very large distances. Based on detailed radiation-hydrodynamics (RHD) simulations of RSGs (Freytag et al. 2002 and Freytag & Höfner 2008), Chiavassa et al. (2009) (Paper I hereafter) and Chiavassa et al. (2010a) (Paper II hereafter) show that these stars are characterised by vigorous convection, which imprints a pronounced granulation pattern on the stellar surface. In particular, RSGs give rise to large granules

that are comparable to the stellar radius in the H and K bands, and an irregular pattern in the optical region.

This paper is the third in the series aimed at exploring the convection in RSGs. The main purpose is to extract photocentric and photometric predictions that will be used to estimate the number of RSGs, detectable by Gaia, for which the parallax measurement will be affected by the displacements of their photometric centroid (hereafter "photocentre").

2. Radiative hydrodynamic simulations of red supergiant stars

The numerical simulation used in this work has been computed with CO^{5}BOLD (Freytag et al. 2002; Freytag & Höfner 2008). The model, extensively introduced in Paper I, has a mass of 12 $M_\odot$, employs an equidistant numerical mesh with 235^3 grid points with a resolution of 8.6 $R_\odot$ (or 0.040 AU), a luminosity average over spherical shells and over time (i.e., over five years) of $L = 93\,000 \pm 1300\ L_\odot$, an effective temperature of $T_{\rm eff} = 3490 \pm 13$ K, a radius of $R = 832 \pm 0.7\ R_\odot$, and a surface gravity $\log g = -0.337 \pm 0.001$. The uncertainties are measures of the temporal fluctuations. This is our most successful RHD simulation so far because it has stellar parameters closest to Betelgeuse ($T_{\rm eff} = 3650$ K, $\log g = 0.0$, Levesque et al. 2005; or $\log g = -0.3$, Harper et al. 2008). We stress that the surface gravity of Betelgeuse is poorly known, and this is not without consequences for the analysis that will be presented in Sect. 6.1 (see especially Fig. 18).

For the computation of the intensity maps and spectra based on snapshots from the RHD simulations, we used the code Optim3D (see Paper I), which takes into account the Doppler shifts caused by the convective motions. The radiative transfer is computed in detail using pre-tabulated extinction coefficients per unit mass generated with MARCS (Gustafsson et al. 2008) as a function of temperature, density, and wavelength for the solar composition (Asplund et al. 2006). The tables include the same extensive atomic and molecular data as the MARCS models. They were constructed with no micro-turbulence broadening, and the temperature and density distributions are optimised to cover the values encountered in the outer layers of the RHD simulations.

3. Predictions

In this section we provide a list of predictions from 3D simulations that are related to the Gaia astrometric and photometric measurements.

3.1. Photocentre variability

We computed spectra and intensity maps in the Gaia G band for the whole simulation-time sequence, namely ~five years with snapshots ~23 days apart. The corresponding spectrum is presented in Fig. 1 and the images in Fig. 2.

Paper II showed that the intensity maps in the optical region show high-contrast patterns that are characterised by dark spots and bright areas. The brightest areas exhibit an intensity 50 times brighter than the dark ones with strong changes over some weeks. Paper II reported robust interferometric comparisons of hydrodynamical simulations with existing observations in the optical and H band regions, which argued for the presence of convective cells of various sizes on the red supergiant Betelgeuse. The Gaia G band images (Fig. 2) are comparable

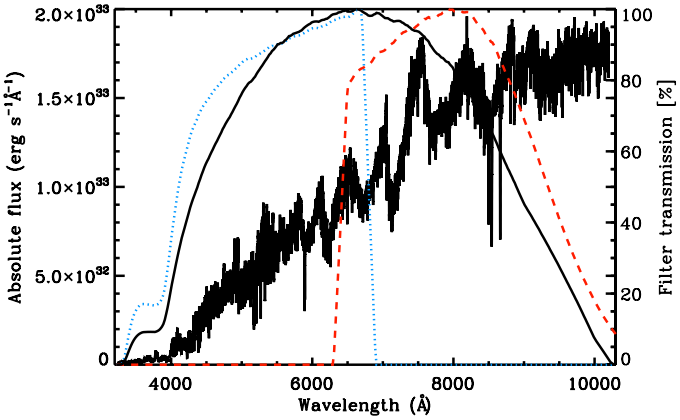

Fig. 1. Transmission curve of the Gaia G band white light passband (solid black line), the blue (dotted blue line) and red (dashed red line) photometric filters (Jordi et al. 2010; Jordi & Carrasco 2007) together with the synthetic spectrum computed from the RHD simulation described in the text.

with what has been found in Paper II. The resulting surface pattern, though related to the underlying granulation pattern, is also connected to dynamical effects. In deed, the emerging intensity depends on (i) the opacity run through the atmosphere (and in red supergiants, TiO molecules produce strong absorption at these wavelengths; see spectrum in Fig. 1) and on (ii) the shocks and waves that dominate at optical depths smaller than 1.

The surface appearance of RSGs in the Gaia G band strongly affects the position of the photocentre and causes temporal fluctuations. The position of the photocentre is given as the intensity-weighted mean of the $x-y$ positions of all emitting points tiling the visible stellar surface according to

$$P_x = \frac{\sum_{i=1}^{N}\sum_{j=1}^{N} I(i,j) * x(i,j)}{\sum_{i=1}^{N}\sum_{j=1}^{N} I(i,j)} \quad (1)$$

$$P_y = \frac{\sum_{i=1}^{N}\sum_{j=1}^{N} I(i,j) * y(i,j)}{\sum_{i=1}^{N}\sum_{j=1}^{N} I(i,j)}, \quad (2)$$

where $I(i,j)$ is the emerging intensity for the grid point (i,j) with coordinates $x(i,j)$, $y(i,j)$ of the simulation, and $N = 235$ is the total number of grid points. Figure 3 shows that the photocentre excursion is large, since it goes from 0.005 to 0.3 AU over five years of simulation (the stellar radius is ~4 AU, Fig. 2). The temporal average value of the photocentre displacement is $\langle P \rangle = \langle (P_x^2 + P_y^2)^{(1/2)} \rangle = 0.132$ AU, and $\sigma_P = 0.065$ AU.

At this point it is important to define the characteristic time scale of the convective-related surface structures. RHD simulations show that RSGs are characterised by two characteristic time scales:

(i) the surface of the RSG is covered by a few large convective cells with a size of about 1.8–2.3 AU (~60% of the stellar radius) that evolve on a *time scale of years* (see Fig. 4 and Paper I). This is visible in the infrared, and particularly in the H band where the H^- continuous opacity minimum occurs and consequently the continuum-forming region is more evident;

(ii) in the optical region, as in Fig. 2, short-lived (*a few weeks to a few months*) small-scale (about 0.2–0.5 AU, ~10% of the stellar radius) structures appear. They result from the opacity run and dynamics at optical depths smaller than 1 (i.e.,

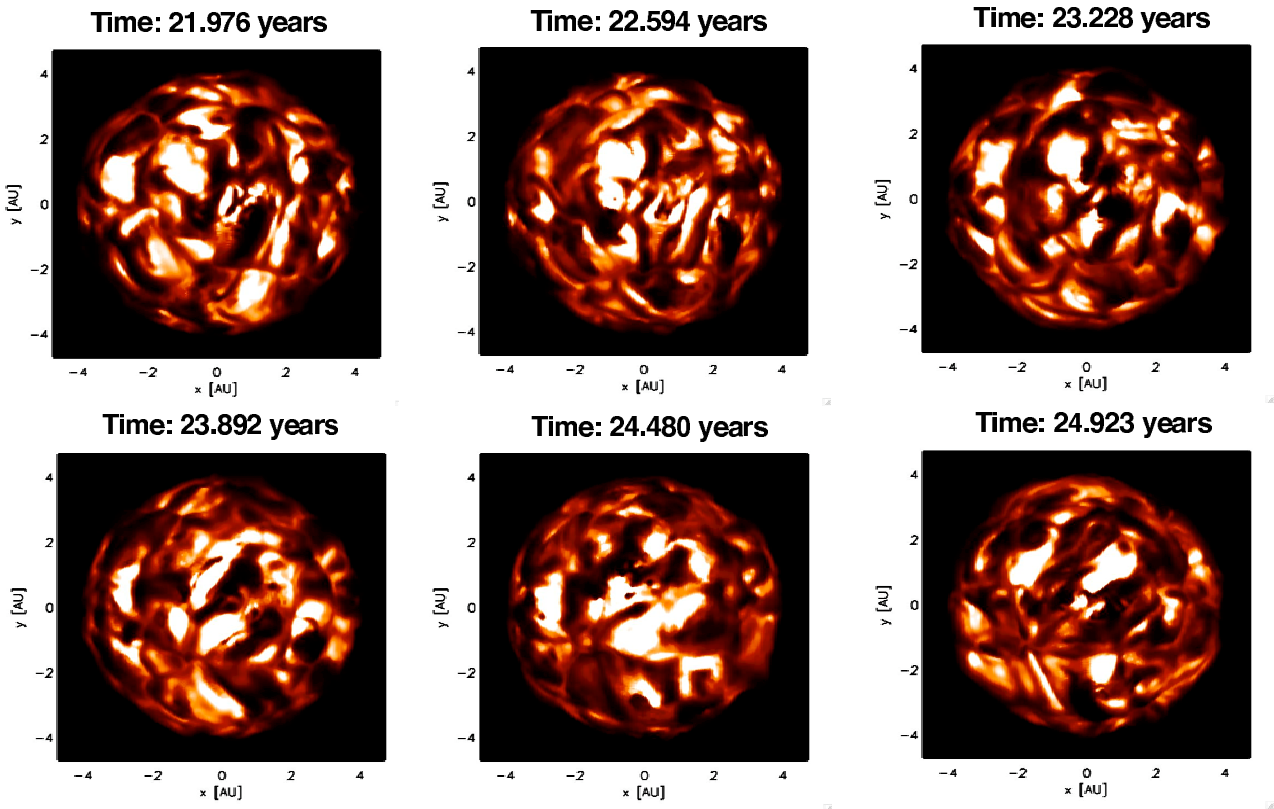

Fig. 2. Maps of the linear intensity (the range is [0–230 000] erg/s/cm^2/Å) in the Gaia G band. Each panel corresponds to a different snapshot of the model described in the text with a step of about 230 days (~five years covered by the simulation).

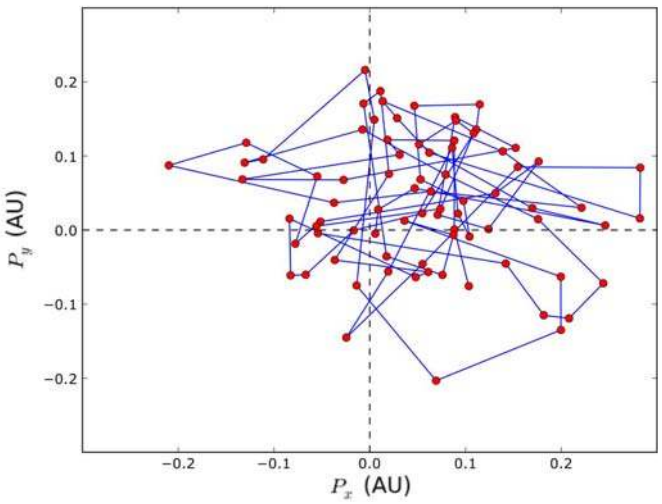

Fig. 3. Photocentre position computed from the snapshots of Fig. 2, in the Gaia G band filter. The total simulated time is ~five years and the snapshots are 23 days apart. The snapshots are connected by the line segments. The dashed lines intersect at the position of the geometrical centre of the images. Note that the photocentric shift stays in the first quadrant for most of the 5 year simulation, and reflects the long lifetime of the large convective cell best visible in the infrared H band (Fig. 4).

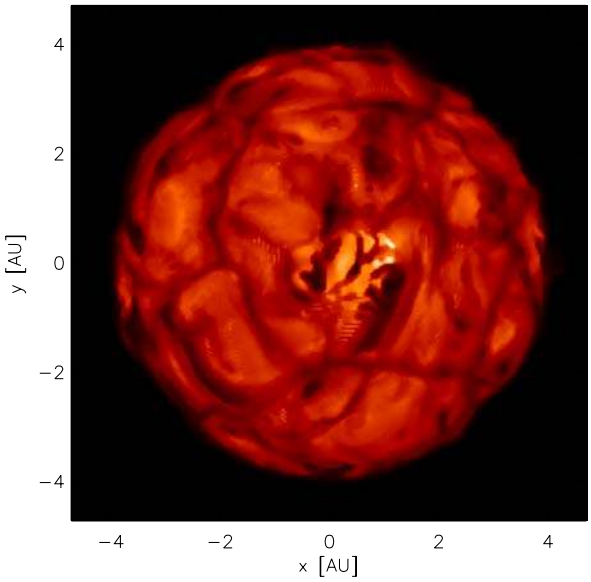

Fig. 4. Map of the linear intensity in the IONIC filter (H band as described in Paper I). The range is [0–3.1 × 10^5] erg cm^{-2} s^{-1} Å^{-1}. The snapshot corresponds to the top left snapshot at t = 21.976 year in Fig. 2. The large convective cell visible in this figure is swamped in smaller-scale photospheric structures in the Gaia G band images.

further up in the atmosphere with respect to the continuum-forming region).

Both time scales have an effect on the photocentre excursion during the five years covered by the simulation. On one hand, the value of σ_P is mostly fixed by the short time scales corresponding to the small atmospheric structures. On the other hand, the fact that $\langle P_x \rangle$ and $\langle P_y \rangle$ do not average to zero (according to Fig. 3, the photocentre stays most of the time in the same quadrant, because of the large convective cell that is visible in the H band; see Fig. 4 and Paper I) indicates that the five year period

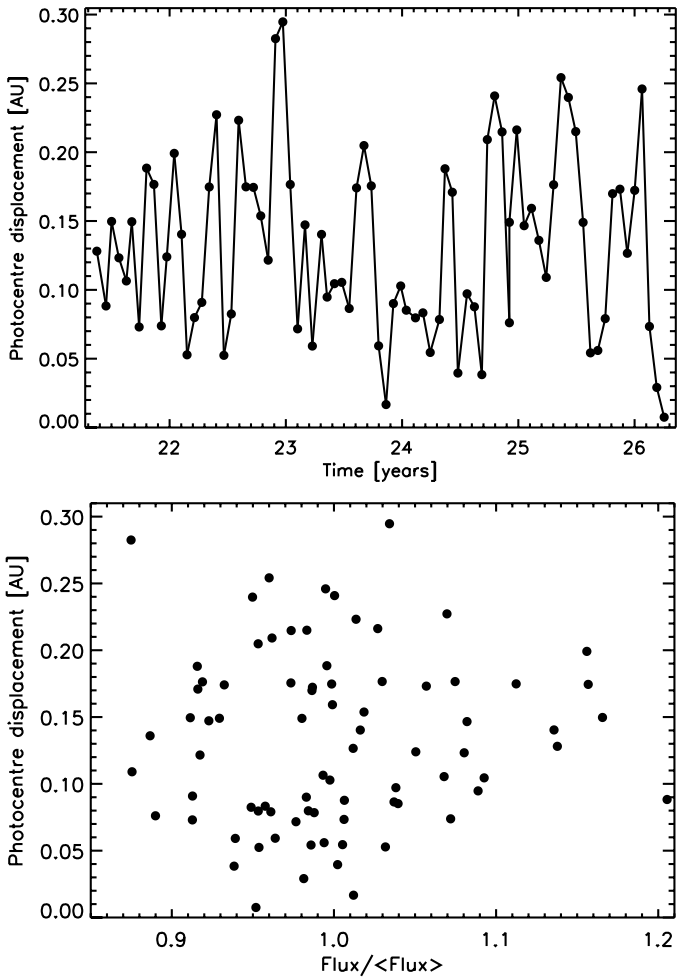

Fig. 5. *Top panel*: modulus of the photocentre displacement as a function of time. *Bottom panel*: photocentre displacement as a function of the integrated flux in the Gaia G band, $\int_{3250\ \text{Å}}^{10300\ \text{Å}} F_\lambda\ \mathrm{d}\lambda$, normalised by the temporal average integrated flux.

covered by the simulation is not yet long enough with respect to the characteristic time scale of the large-scale (continuum) cells.

The top panel of Fig. 5 shows the temporal photocentre displacement over the ∼five years of simulation, which is comparable to the total length of the Gaia mission. As seen in the figure, for $t < 22$ year, the random displacement is small and increases to a maximum value of 0.30 AU at $t \sim 23$ year.

In relation with the astrometric implications of this photocentre displacement, which will be discussed in Sect. 4, it must be stressed that neither $\langle P \rangle$ nor σ_P (the latter corresponding to the time sampling of the photocentric motion with a rather arbitrary time interval of 23 days) are the relevant quantities; it is instead the standard deviation of P sampled as Gaia will do (both timewise and directionwise), which turns out to be relevant. This quantity is computed below.

The bottom panel of Fig. 5 shows that there is no obvious correlation between the photocentre variability and the emerging intensity integrated in the Gaia G band. Ludwig (2006) showed analytically that this lack of correlation is to be expected.

Gaia will scan the sky, observing each object on average 70−80 times. The main information that will be used to determine the astrometric characteristics of each stars will be the along-scan (AL) measurement. This is basically the projection of the star position along the scanning direction of the satellite with respect to a known reference point. By fitting those data through a least-squares minimisation, the position, parallax, and proper motion of the star can be derived. The possibility of extracting these parameters is ensured by Gaia's complex scanning law[1], which guarantees that every star is observed from many different scanning angles.

In presence of surface brightness asymmetries the photocentre position will not coincide with the barycentre of the star and its position will change as the surface pattern changes with time. The result of this phenomenon is that the AL measurements of Gaia will reflect proper motion, parallactic motion (that are modelled to obtain the astrometric parameters of the star) and photocentric motion of convective origin. The presence of the latter will be regarded as a source of additional noise.

The impact of those photocentre fluctuations on the astrometric quantities will depend on several parameters, some of which are the stellar distance and the time sampling (fixed by the scanning law) of the photocentric motion displayed in Fig. 3. To better assess this impact, we proceeded as follows. The Gaia Simulator (Luri et al. 2005) was used to derive scanning angles and time sampling for stars regularly spaced (one degree apart) along the galactic plane where the supergiants are found. We computed the photocentre coordinates at the Gaia transit times by linear interpolation of the photocentre positions of the model (as provided by Fig. 3), after subtracting $\langle P_x \rangle$ (=0.055 AU) and $\langle P_y \rangle$ (=0.037 AU; as we will explain below, a constant photocentric offset has no astrometric impact on the parallax). We then computed their projection on the AL direction, which we denote P_θ, θ being the position angle along the scanning direction on the sky. This projection P_θ relates to the modulus P of the photocentre vector plotted in Fig. 5 through the relation

$$P_\theta = P\cos(\theta - \theta_P) \quad \text{with} \quad \tan\theta_P = \left(P_y - \langle P_y \rangle\right) / \left(P_x - \langle P_x \rangle\right), \tag{3}$$

and similarly, we define

$$P'_\theta = P\cos(\theta - \theta'_P) \quad \text{with} \quad \tan\theta'_P = P_y/P_x. \tag{4}$$

The resulting run of the standard deviation of the photocentre displacement with time for two representative stars (one located at $l = 0°$ with 59 transits and the other located at $l = 241°$ with 227 transits) is shown in Fig. 6, which reveals that the time sampling is, as expected, strongly dependent upon the star position on the sky. The transits separated by $2{-}6{\times}10^{-4}$ years correspond to the star being observed in succession by the two fields of view (separated by 106.5 degrees on the sky) by the satellite spinning at a rate of six hours per cycle, whereas the longer intervals are fixed by the satellite precession rate.

Finally, we computed the standard deviation of those projections, and obtained σ_{P_θ} values ranging from 0.06 to 0.10 AU (Fig 7), with $\langle |P_\theta| \rangle$ ranging from $1{\times}10^{-4}$ to $8{\times}10^{-2}$ AU. In the remainder of this paper, we will adopt $\sigma_{P_\theta} = 0.08$ AU. This quantity, which represents about 2.0% of the stellar radius (∼4 AU; Sect. 2), is a measure of the mean photocentre noise induced by the convective cells in the model, and it is this value that needs to be compared with the Gaia or Hipparcos measurement uncertainty to evaluate the impact of granulation noise on the astrometric parameters. This will be done in Sects. 4 and 5.

We note that $\sigma_{P_\theta} = 0.08$ AU is in fact larger than $\sigma_P = 0.065$ AU, and this can be understood as follows. First, from

[1] See http://www.rssd.esa.int/index.php?project=GAIA&page=picture_of_the_week&pow=13

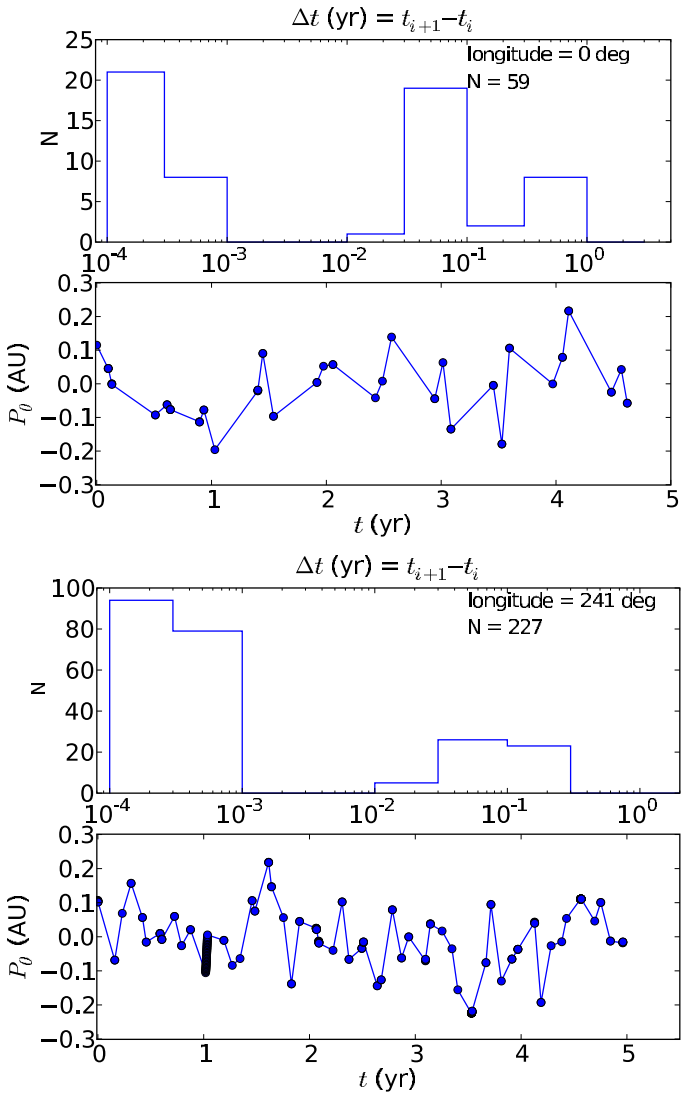

Fig. 6. Along-scan photocentre displacement P_θ (in AU) against time for two different samplings of the photocentre displacement of Fig. 3, corresponding to the Gaia scanning law applied to stars located along the galactic plane at longitudes of 0° and 241°, as indicated on the figures. The top panel of each pair provides the distribution of time intervals between successive measurements.

Eq. (4) and basic statistical principles, the following relation may be easily demonstrated:

$$\sigma^2_{P'_\theta} = 0.5\ (\sigma^2_P + \langle P\rangle^2), \tag{5}$$

under the obvious hypothesis of statistical independence between the scanning directions θ and the photocentric positions P_x, P_y. With $\langle P\rangle = 0.132$ AU, and $\sigma_P = 0.065$ AU obtained in Sect. 3.1, the above relation predicts $\sigma_{P'_\theta} = 0.10$ AU, in agreement with the actual predictions based on Eq. (4). If one considers instead P_θ from Eq. (3) (thus projecting the 're-centred' photocentric displacement), there is a small reduction of the standard deviation according to

$$\sigma^2_{P_\theta} = \sigma^2_{P'_\theta} - 0.5(\langle P_x\rangle^2 + \langle P_y\rangle^2), \tag{6}$$

yielding $\sigma_{P_\theta} = 0.088$ AU, in agreement with the detailed calculations shown in Fig. 7.

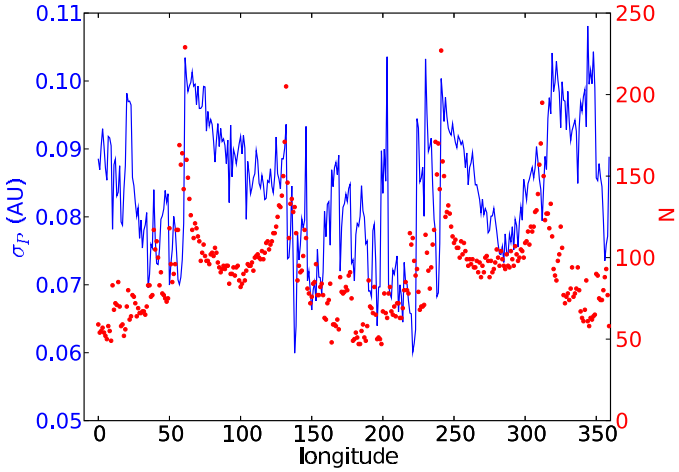

Fig. 7. Run of σ_{P_θ} (expressed in AU; solid blue curve and left-hand scale) with galactic longitude for stars located along the galactic plane, with a number of transit observations given by the red dots (and right-hand scale).

3.2. Photometric variability

Another aspect of RSG variability can affect Gaia spectrophotometry. The blue and red photometric bands of Fig. 1 produce two spectra of the observed source at low spectral resolution ($R \sim 50$). The photometric system has the advantage of continuously covering a wide range of wavelengths providing a multitude of photometric bands, but it has the great disadvantage of being extremely hard to calibrate in flux and wavelength. The photometric system of Gaia will be used to characterise the star's effective temperature, surface gravity, and metallicity (Thévenin 2008). The vigorous convective motions and the resulting surface asymmetries of RSGs cause strong fluctuations in the spectra that will affect Gaia spectrophotometric measurements (Fig. 8). In the blue photometric range (top panel), the fluctuations go up to 0.28 mag and up to 0.15 mag in the red filter (bottom panel) over the five years of simulation. These values are of the same order as the standard deviation of the visible magnitude excursion in the last 70 years for Betelgeuse, 0.28 mag (according to AAVSO[2]).

The light curve of the simulation in the (blue - red) Gaia colour index is displayed in Fig. 9. The temporal average value of the colour index is (blue -red)= 3.39 ± 0.06 at one sigma and there are some extreme values at, for example, $t \sim 22.4$ year, $t \sim 23$ year, and $t \sim 25.2$ year.

Therefore, the uncertainties on [Fe/H], $T_{\rm eff}$, and $\log g$ given by Bailer-Jones (2010) for stars with $G < 15$ should be revised upwards for RSGs because of temporal fluctuations from convection.

3.3. Direct imaging and interferometric observables

The simulation presented in this work was already tested against the observations at different wavelengths including the optical region (Papers I and II). However, it is now also possible to compare the predictions in the Gaia G band to CHARA interferometric observations obtained with the new instrument VEGA (Mourard et al. 2009) that is integrated within the CHARA array at Mount Wilson Observatory. For this purpose, we computed intensity maps in the blue and red bands of Fig. 1 and

[2] American Association of Variable Star Observers, www.aavso.org

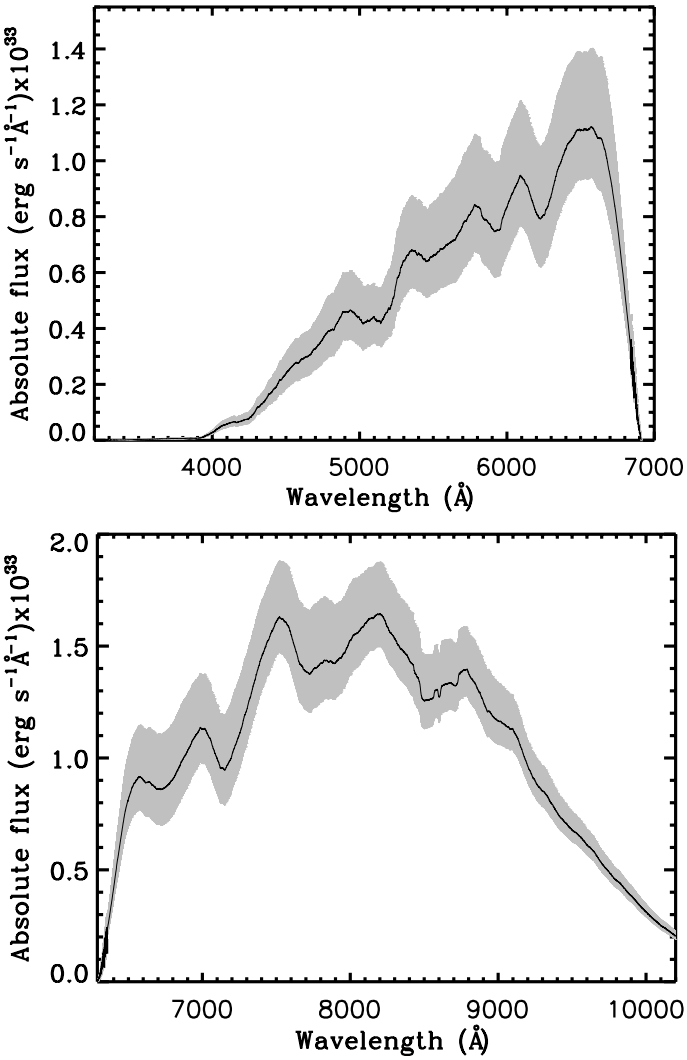

Fig. 8. Spectral fluctuations in the blue and red Gaia photometric bands (Fig. 1) for RSGs: the black curve is the average flux over ∼five years covered by the simulation, while the grey shade denotes the maximum and minimum fluctuations. The spectra were smoothed to the Gaia spectral resolution ($R \sim 50$, Thévenin 2008).

calculated visibility curves for 36 different position angles with a step of 5° following the method explained in Paper I. Figure 10 shows the intensity maps together with the corresponding visibility curves. The angular visibility fluctuations are larger in the blue band (bottom left panel) because there is a larger contribution from molecular opacities (mainly TiO) that shade the continuum brightness of the star (top left panel): therefore the surface brightness contrast is higher. However, in both photometric bands the signal in the second lobe, at higher frequencies, is ∼0.2 dex higher than the uniform disc (UD) result, which is measurable with CHARA.

The approach we suggest to follow in order to check the reliability of the 3D simulation is the following: to search for angular visibility variations, as a function of wavelength, observing with the same telescope configuration covering high spatial frequencies and using the Earth's rotation to study 6–7 different position angles in one night. The error bar should be kept smaller than the predicted fluctuations: ∼40% in the blue band, and ∼20% in the red band at the peak of the second visibility lobe.

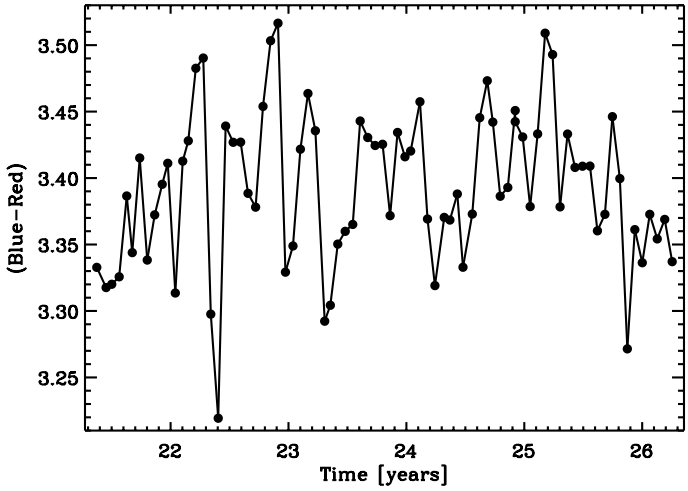

Fig. 9. (blue – red) Gaia colour index, computed in the blue and red photometric filters of Fig. 1, as a function of time.

To investigate the behaviour of the local flux fluctuations, closure phases will bring invaluable information on the asymmetry of the source. However, the final consistency check will be an image reconstruction to directly compare the granulation size and shape and the intensity contrast, provided by the planned second generation recombiner of the VLTI and CHARA optical interferometry arrays. The European Extremely Large Telescope (E-ELT, planned to be operating in 2018) with a mirror size five times larger than a single VLT Unit Telescope will be capable of near IR observations of surface details on RSGs (Fig. 11).

4. Impact of photocentric noise on astrometric measurements

The basic operating mode of astrometric satellites like Hipparcos or Gaia is to scan the sky and to obtain along-scan[3] positions $\eta_{\rm AL}$, as was already briefly sketched in Sect. 3.1. The core astrometric data analysis then consists in solving a least-squares problem (for the sake of simplicity, we neglect the AC term) (Lindegren 2010)

$$\min_{\boldsymbol{p},\,\boldsymbol{a}} \left(\sum_{i}^{N_{\rm transit}} \frac{[\eta_i - \eta(\boldsymbol{p},\boldsymbol{a};t_i)]^2}{\sigma^2_{\eta_i}} \right) \tag{7}$$

for the astrometric parameters $\boldsymbol{p}$, and the set of satellite attitude parameters $\boldsymbol{a}$, given the $N_{\rm transit}$ along-scan positions η_i at times t_i, the model predictions $\eta(\boldsymbol{p},\boldsymbol{a};t_i)$, and the formal error σ_{η_i} on the along-scan position η_i (including centroiding errors and errors caused by imperfect calibration or imperfectly known satellite attitude for instance). If η_i is affected by some supplementary noise coming from the photocentric motion (which is not going to be included in σ_{η_i}), then this photocentric noise of variance $\sigma^2_{P_\theta}$ will degrade the goodness-of-fit in a significant manner, provided that $\sigma_{P_\theta} \gtrsim \sigma_\eta$. This statement is easily demonstrated from Eq. (7), by writing $\eta_i = \tilde{\eta}_i + P_{\theta_i}$, with the first term $\tilde{\eta}_i$ representing the astrometric motion, and the second term representing the along-scan photocentric shift:

$$\chi^2 \equiv \sum_{i=1}^{N_{\rm transit}} \frac{[\tilde{\eta}_i + P_{\theta_i} - \eta(\boldsymbol{p},\boldsymbol{a};t_i)]^2}{\sigma^2_{\eta_i}}. \tag{8}$$

[3] Across-scan (AC) measurements will be obtained as well by Gaia, but will have a lower precision.

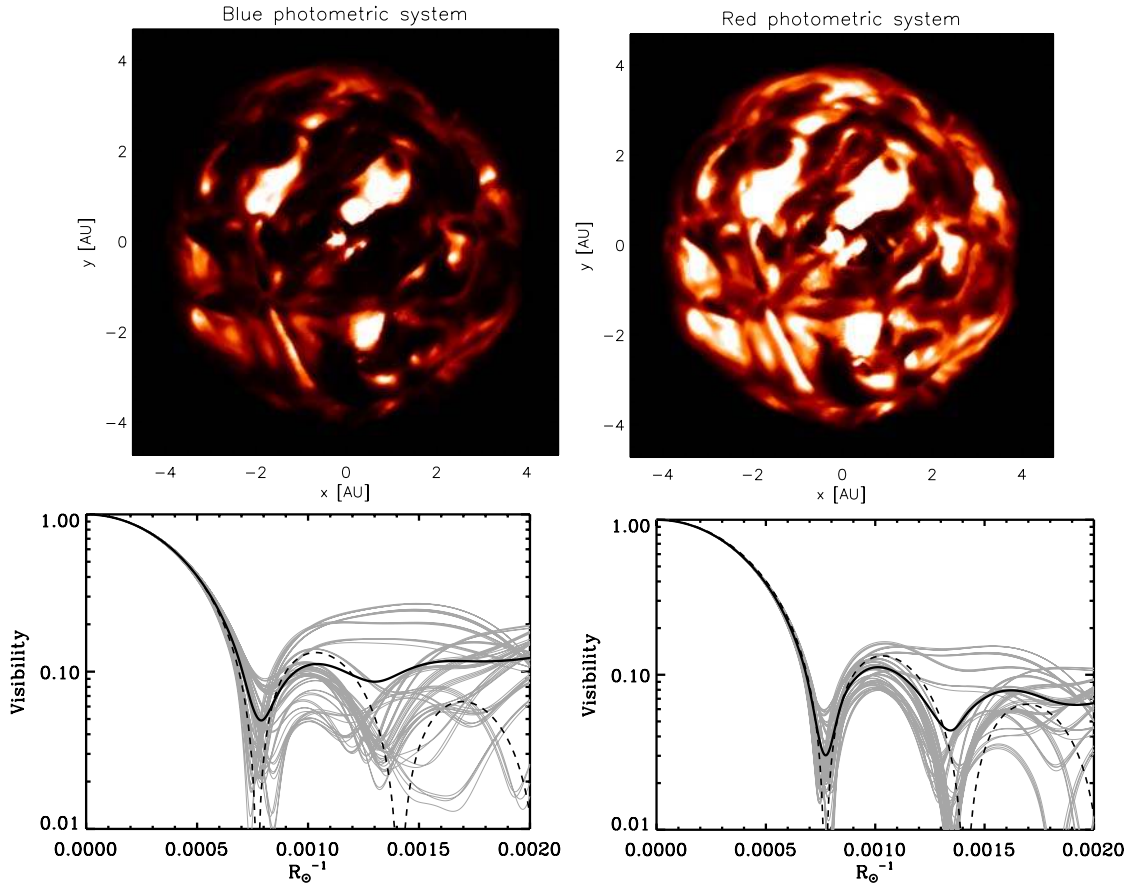

Fig. 10. *Top panels*: maps of the linear intensity (the range is [0–230 000] erg/s/cm^2/Å) computed in the blue and red photometric filters of Fig. 1. *Bottom panels*: visibility curves from the above maps computed for 36 different position angles 5° apart (grey lines). The black curve is the average visibility, while the dashed line is a uniform disc of about the same radius as the simulation snapshot. The conversion factor to the more customary unit arcsec^{-1} on the abscissa axis is arcsec^{-1} = $R_\odot^{-1} d$ [pc] 214.9 (see Paper I).

For the sake of simplicity, we will assume below that σ_η is the same for all measurements. The above equation may be further simplified in the case where there is no correlation between the astrometric and photocentric shifts, so that the cross-product term $\sum_{k=1}^{N_{\rm transit}} (\tilde{\eta_k} - \eta(\boldsymbol{p}, \boldsymbol{a}; t_k))\ P_{\theta_k}$ is null. This absence of correlation only holds if the photocentric shift occurs on time scales different from one year (no correlation with the parallax), and shorter than a few years (no correlation with the proper motion[4]). Although this assumption of absence of correlation turns out not to be satisfied in real cases (we will return to this issue in the discussion of Fig. 21), it nevertheless offers insights into the situation, and we therefore pursue the analytical developments by writing

$$\chi^2 = \frac{1}{\sigma_\eta^2}\left[\sum_{i=1}^{N_{\rm transit}} [\tilde{\eta}_i - \eta(\boldsymbol{p}, \boldsymbol{a}; t_i)]^2 + \sum_{i=1}^{N_{\rm transit}} P_{\theta_i}^2\right] = \chi_0^2 + N_{\rm transit}\ \frac{\sigma_{P_\theta}^2}{\sigma_\eta^2}, \quad (9)$$

where χ_0^2 is the chi-square obtained in the absence of photocentric motion, and we assumed $\sigma_{P_\theta}^2 = (1/N_{\rm transit}) \sum_{k=1}^{N_{\rm transit}} P_{\theta_k}^2$ since asymptotically $\langle P_\theta \rangle = 0$. It is important to stress here that it is indeed the standard deviation of the photocentre displacement (*sampled the same way as the astrometric data have been*) – rather than its average value – that matters. In the extreme case of a constant (non-zero) photocentre shift, there will obviously be no impact on the astrometric parameters.

[4] The large subphotospheric convective cells lead to conspicuous spots in the infrared bands, which move on time scales of several years (Paper I). However, in the optical bands, these large spots are not as clearly visible, since they are swamped in smaller-scale photospheric structures.

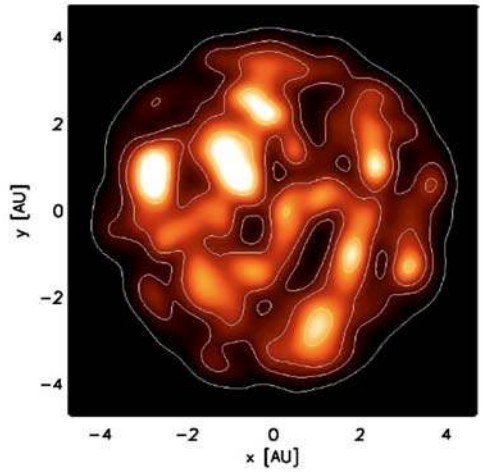

Fig. 11. Snapshot of 3D simulation (*upper left* of Fig. 2) convolved to the PSF of a 42 m telescope (for a star at a distance of 152.4 pc, see solution #2 in Table 2) like the European Extremely Large Telescope.

The degradation of the fit caused by the photocentric noise may be quantified through the goodness-of-fit parameter $F2$, defined as

$$F2 = \left(\frac{9\nu}{2}\right)^{1/2}\left[\left(\frac{\chi^2}{\nu}\right)^{1/3} + \frac{2}{9\nu} - 1\right], \tag{10}$$

where ν is the number of degrees of freedom of the χ^2 variable. The above definition corresponds to the "cube-root transformation" of the χ^2 variable (Stuart & Ord 1994). The transformation of (χ^2, ν) to $F2$ eliminates the inconvenience of having the distribution depending on the additional variable ν, which is not the same for the different stars. $F2$ follows a normal distribution with zero mean and unit standard deviation. The goodness-of-fit $F2$ thus appears to be an efficient way to detect any photocentric noise. It may be compared to its value $F2_0$ in the absence of photocentric noise by assuming $\chi_0^2/\nu = 1$ and $N_{\rm transit}/\nu \sim 1$; then Eq. (9) writes

$$\chi^2 \sim \chi_0^2\left(1 + \frac{N_{\rm transit}}{\nu}\,\frac{\sigma_{P_\theta}^2}{\sigma_\eta^2}\right), \tag{11}$$

thus leading to

$$F2 = F2_0 + \left(\frac{9\nu}{2}\right)^{1/2}\left[\left(1 + \frac{\sigma_{P_\theta}^2}{\sigma_\eta^2}\right)^{1/3} - 1\right]. \tag{12}$$

For Gaia, the second term of the above equation may be evaluated as a function of $\sigma_{P_\theta}/\sigma_\eta$ by adopting $\nu = 70$, as represented in Fig. 12. Because $F2$ follows a normal distribution with zero mean and unit standard deviation, the fit degradation will become noticeable if $F2$ increases by 2 or so, implying $\sigma_{P_\theta}/\sigma_\eta \gtrsim 0.6$. This translates into a condition on the distance:

$$d\ [\mathrm{kpc}] \lesssim \frac{\sigma_{P_\theta}\ [\mathrm{AU}]}{0.6\ \sigma_\eta\ [\mathrm{mas}]}. \tag{13}$$

The error on the along-scan position η should not be confused with the end-of-mission error on the parallax (σ_ϖ), which ultimately results from the combination of $N_{\rm transit}$ transits, with $N_{\rm transit}$ ranging from 59 to 120 for Gaia, with an average of $\bar{N}_{\rm transit} = 78$ (Lindegren 2010), and from 10 to 75 for Hipparcos (Fig. 3.2.4 of Vol. 1 of the Hipparcos and Tycho Catalogues). The number of transits depends (mostly) on the ecliptic latitude.

For Hipparcos, the individual σ_η values for each transit may be found in the Astrometric Data files (van Leeuwen & Evans 1998; van Leeuwen 2007a), and are of the order of 1.7 mas for the brightest stars (see Sect. 5 and Fig. 15). For Gaia, the quantity σ_η may be obtained from the relation

$$\sigma_\eta = \frac{N_{\rm transit}^{1/2}}{m\, g_{\rm par}}\,\sigma_\varpi, \tag{14}$$

where $m = 1.2$ denotes an overall end-of-mission contingency margin, and $g_{\rm par} = 1.91$ is a dimensionless geometrical factor depending on the scanning law, and accounting for the variation of $N_{\rm transit}$ across the sky, since σ_ϖ is an effective sky-average value (see de Bruijne 2005). A current estimate of σ_ϖ is 7.8 μas for the brightest stars (Lindegren 2010), yielding σ_η of the order of 30 μas. To avoid saturation on objects brighter than $G = 12.6$, a special CCD gating strategy will be implemented so that the error budget may be assumed to be a constant for $G \leq 12.6$ (de Bruijne 2005; Lindegren 2010). As we show in Sect. 6, only the bright-star regime matters for our purpose. Inserting these values in Eq. (13), we thus find

$$d\ [\mathrm{kpc}] \leq 0.98\ \sigma_{P_\theta}\ [\mathrm{AU}] \qquad \text{for Hipparcos,} \tag{15}$$

and

$$d\ [\mathrm{kpc}] \leq 55.5\ \sigma_{P_\theta}\ [\mathrm{AU}] \qquad \text{for Gaia.} \tag{16}$$

Adopting $\sigma_{P_\theta} = 0.08$ AU for Betelgeuse-like supergiants (Sect. 3.1) yields $d < 0.08$ kpc for Hipparcos and $d < 4.4$ kpc for Gaia. This limit has to be interpreted as marking the maximum distance up to which a photocentric motion with $\sigma_{P_\theta} = 0.08$ AU will increase the astrometry goodness-of-fit by 2. The validity of these conditions will be further evaluated in Sects. 5 and 6.

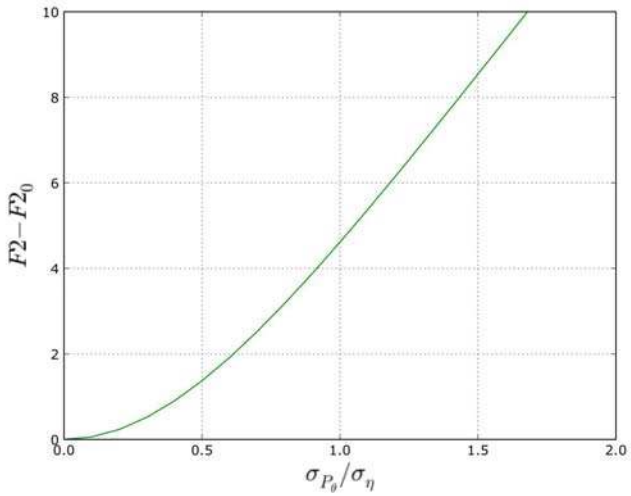

Fig. 12. Degradation of the goodness-of-fit $F2$ in the presence of a photocentric motion described in terms of the ratio $\sigma_{P_\theta}/\sigma_\eta$, where σ_η is the instrumental error. Remember that $F2$ follows a normal distribution with zero mean and unit standard deviation.

With this photocentric noise, the astrometric data reduction process may adopt one of the following three approaches:

(i) Neither the model definition, nor the measurement-error definition are modified (meaning that the quantities σ_i entering Eq. (9) are the same as before, and that no attempt is whatsoever made to model the granulation). With respect to a star with similar properties (same apparent magnitude and location on the sky), a star with global-scale convection cells will then be recognised by a goodness-of-fit $F2$ value higher than expected depending upon the ratio $\sigma_{P_\theta}/\sigma_\eta$ (see Fig. 12). Under those conditions, the resulting *formal* uncertainty on the parallax would *not* be especially large, though; actually, it would be exactly identical to the parallax uncertainty in the absence of photocentric motion. This is because the formal errors on the parameters $\boldsymbol{p}$ (among which the parallax) only depend on the measurement errors σ_η (which were kept the same with or without photocentric noise), and not on the actual measured values (which will be different in the two situations). This is demonstrated in Appendix A. But of course, the error on the parallax derived in this way is underestimated, because it does not include the extra source of noise introduced by the photocentric motion. The next possibility alleviates this difficulty.

(ii) An estimate of the photocentric noise may be quadratically added to σ_η^2 appearing in Eq. (8). The error on the parallax will then be correctly estimated (and will be larger than the one applying to similar non-convective stars); the

Table 1. Properties of the spots observed at the surface of Betelgeuse during the Hipparcos mission.

	Spot 1			Spot 2			Photocentre	
	pos. offset [mas]	pos. angle [°]	flux fraction %	pos. offset [mas]	pos. angle [°]	flux fraction %	pos. offset [mas]	pos. angle [°]
January 1991	9 ± 2	105 ± 3	12 ± 2	9 ± 2	305 ± 4	11 ± 2	**0.4**	**39**
January 1992	2 ± 1	40 ± 10	17 ± 2	29 ± 3	–45 ± 5	4 ± 1	**1.2**	**–29**

Notes. The position offset refers to the centre of the extended disc, of radius 27 mas (Jan. 1991) and 23 mas (Jan. 1992). Data from Wilson et al. (1992); Tuthill et al. (1997).

goodness-of-fit will no longer be unusually large. This is the method adopted for the so-called "stochastic solutions" in the Hipparcos reduction, an example of which will be presented in Sect. 5. These solutions, called "DMSA/X", added some extra-noise (in the present case: the photocentric noise) to the measurements to get an acceptable fit.

(iii) The model is modified to include the photocentric motion. This would be the best solution in principle, because it would allow us to alleviate any possible error on the parallax, as they may occur with the two solutions above. However, the 3D simulations reveal that it is very difficult to model the complex convective features seen in visible photometric bands by a small number of spots with a smooth time behaviour. This solution was therefore not been attempted.

The astrometric parameters themselves may change of course, for either of the above solutions, especially when the photocentric motion adds to the parallactic motion a signal with a characteristic time scale close to one year. If on the contrary, the photocentric motion has a characteristic time scale very different from one year, the photocentric motion averages out and leaves no imprint on the parallax. A similar situation is encountered if there is an unrecognized orbital motion on top of the parallactic motion: only if the unaccounted orbital signal has a period close to one year will the parallax be strongly affected (see Pourbaix & Jorissen 2000, for a discussion of specific cases). As explained in Sect. 3.1, RSGs large convective cells evolve over time scales of years. In addition, they slightly change their position on the stellar surface within the five years of simulated time (Chiavassa PhD Thesis[5]), but, unfortunately, it is difficult to measure the granule size exactly (Berger et al. 2010) and consequently to give a consistent estimate of this displacement.

5. A look at Betelgeuse's Hipparcos parallax

Hipparcos data (ESA 1997) may hold signatures of global-scale granulation in supergiants. The three nearby supergiants α Sco (Antares; HIP 80763), α Ori (Betelgeuse; HIP 27989) and α Her (Rasalgethi; HIP 84345) are ideal targets for this purpose, since Tuthill et al. (1997) indeed found surface features on all three stars, implying photocentric displacements of the order of 1 mas (estimated from the product of the fraction of flux belonging to a bright spot with its radial distance from the geometric centre; see Table 1). By chance, observations of the disc of Betelgeuse at the time of the Hipparcos mission were done by Wilson et al. (1992) and Tuthill et al. (1997) and are shown in Fig. 13. Tuthill et al. reveal that the two bright spots present in January 1991 merged one a year later (January 1992), with a much fainter spot appearing at the edge of the extended disc. Because the simulation used

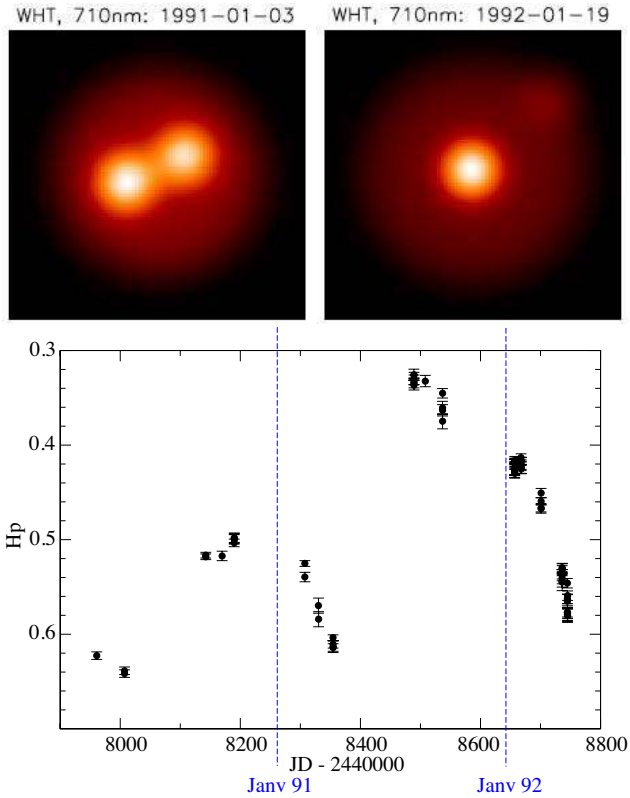

Fig. 13. *Top panel*: interferometric observations of the surface of Betelgeuse obtained with the William Herschel Telescope at a wavelength of 710 nm, in January 1991 (Wilson et al. 1992) and January 1992 (Tuthill et al. 1997). North is at the top and East is to the left. The two images have been taken from Freytag et al. (2002). The spot properties are summarised in Table 1. *Bottom panel*: Hipparcos epoch photometry of Betelgeuse with the vertical lines indicating the epoch of the two interferometric observations.

in this work shows excellent fits to the visibility curves, closure phases, and reconstructed images based on William Herschel Telescope data in the same filters as those used in Fig. 13, and because RSGs are slow rotators, it is most likely that the spots in Fig. 13 are caused by convection. Their properties have been summarised in Table 1, along with the corresponding photocentric displacement. The observed photocentric displacements agree with the model predictions, as can be evaluated from $\sigma_{P_\theta}[\mathrm{mas}] = \sigma_{P_\theta}[\mathrm{AU}] \times \varpi[\mathrm{mas}] = 0.5$ mas, since $\sigma_{P_\theta} = 0.08$ AU for a supergiant (Sect. 4) and $\varpi = 6.56 \pm 0.83$ mas for Betelgeuse (see Table 2; in the remainder of this section, all quantities from Hipparcos refer to van Leeuwen's new reduction, 2007b).

[5] http://tel.archives-ouvertes.fr/docs/00/29/10/74/PDF/Chiavassa_PhD.pdf

Table 2. Parallaxes for Betelgeuse computed from various data sets.

#	Data	N	Δt [year]	ϖ [mas]	Distance [pc]
1	Hipparcos (FAST+NDAC reduction consortia)	38	2.1	7.63 ± 1.64	$131.1^{+35.8}_{-23.2}$
2	van Leeuwen (2007b)	38	2.1	6.56 ± 0.83	$152.4^{+17.1}_{-22.0}$
3	Harper et al. (2008)	51	22.4	5.07 ± 1.10	$197.2^{+35.1}_{-54.6}$

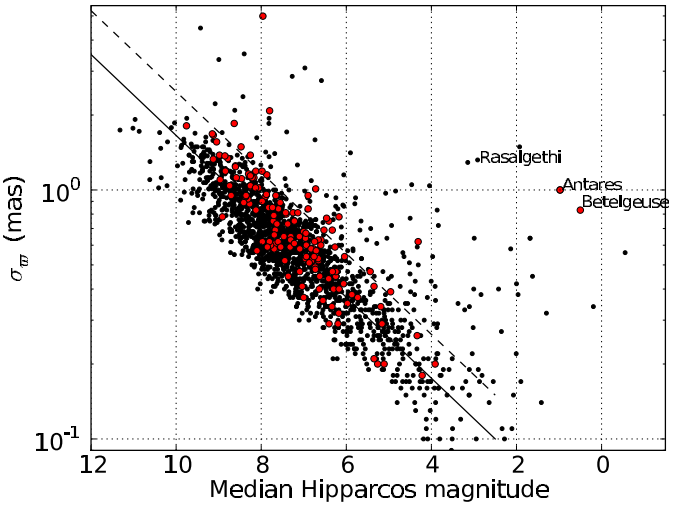

Fig. 14. Parallax standard errors for supergiants in the Hipparcos Catalogue, after van Leeuwen's reprocessing. The dashed line represents 1.5 times the standard parallax error for stars with precise parallaxes (<10%; solid line) in van Leeuwen's reprocessing (see Fig. 2.19 of van Leeuwen 2007a), whereas the solid line represents the fiducial relation between the Hipparcos magnitude and the standard parallax error. Large red circles correspond to stars redder than $V - I = 2$.

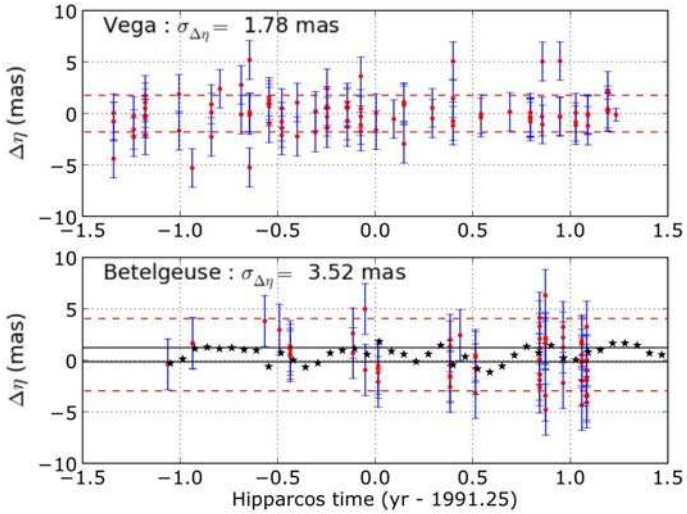

Fig. 15. Abscissa residuals $\Delta\eta$ (in mas on the sky; red dots) along with the corresponding error bar from van Leeuwen (2007a) for Betelgeuse and Vega, as a function of time, expressed in years from 1991.25. Filled star symbols correspond to the along-scan projections P_θ of the synthetic photocentre displacements of Fig. 3. The red dashed lines and black solid lines depict the $\pm 1\sigma$ interval around the mean for the Hipparcos data points and model predictions, respectively. Note that these displacements were computed in the Gaia G filter instead of the Hipparcos Hp filter. A test on a given snapshot has shown that the difference is negligible: $P_x = 0.11$ AU with the Hp filter, as compared to 0.13 AU with the G filter.

Considering that the instrumental uncertainty on an individual measurement is 1.9 mas for a star like Vega ($V = 0.03$), which is as bright as Betelgeuse ($V = 0.42$) (according to Vega's intermediate astrometric data file in van Leeuwen 2007a), Betelgeuse's convective noise with $\sigma_{P_\theta} = 0.5$ mas should be just noticeable on top of the instrumental noise, and possibly have some detectable impact on the astrometric data of Betelgeuse. For Vega, van Leeuwen (2007a) found a very good astrometric solution, whose residuals $\Delta\eta$ have a standard deviation $\sigma_{\Delta\eta}$ of 1.78 mas, fully consistent with the formal errors on η (top panel of Fig. 15). The extreme brightness of Vega thus did not prevent us from finding a good astrometric solution. On the other hand, neither the original Hipparcos processing nor van Leeuwen's revised processing could find an acceptable fit to the Betelgeuse and Antares astrometric data, and a so-called "stochastic solution" (DMSA/X) had to be adopted (the kind of solution labelled (ii) in the discussion of Sect. 4), meaning that some supplementary noise (called "cosmic noise") had to be added to yield acceptable goodness-of-fit values $F2$.

The cosmic noise amounts to 2.4 and 3.6 mas for Betelgeuse and Antares, respectively, in van Leeuwen's reprocessing. These values correspond to the size of the error bars displayed in Figs. 15 and 16. Rasalgethi was not flagged as DMSA/X, but rather as DMSA/C (indicating the presence of a close companion), but its high goodness-of-fit value $F2 = 46.63$ is indicative also of increased noise. Consequently, all three supergiants have a parallax standard error larger than expected[6] given its Hipparcos magnitude Hp, as revealed by Fig. 14, which displays σ_ϖ against the median magnitude for all supergiants (luminosity classes I and II, of all spectral types) in the Hipparcos catalogue. The chromaticity correction has been a serious concern for the reduction of the Hipparcos data of very red stars (see Platais et al. 2003, for a detailed discussion of this problem), and one may wonder whether the increased noise of the three supergiants under consideration could perhaps be related to this effect. Because the very red supergiants (with $V - I > 2.0$) show no appreciable offset from the rest of the sample in Fig. 14 (at least for the brightest supergiants, down to Hp = 8), this possibility may be discarded, and the different behaviour of Rasalgethi,

[6] This larger parallax standard error does not contradict Appendix A stating that, in the presence of a photocentric noise, the standard error on the parallax should stay the same. This is because this parallax standard error is obtained in the framework of a DMSA/X ("stochastic") solution, where the measurement errors were artificially increased by a "cosmic noise" to get an acceptable goodness-of-fit value. Hence, the "design matrix" defined in Appendix A, which is directly related to the variance-covariance matrix of the astrometric parameters, *has* been changed to produce the stochastic solution, thus resulting in a larger parallax error. This corresponds to a solution of kind (ii) in Sect. 4.

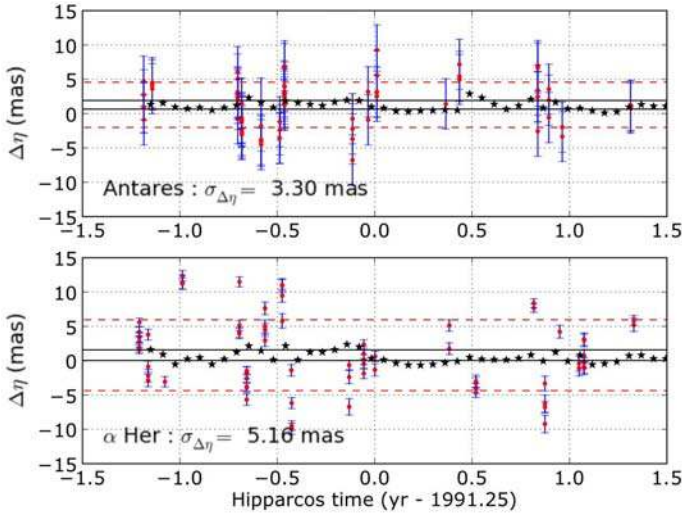

Fig. 16. Same as Fig. 15 for Antares and α Her.

Antares, and Betelgeuse in Fig. 14 seems instead related to their large apparent brightness, which is caused by their proximity to the Sun.

Could the poor accuracy of Betelgeuse's parallax and its cosmic noise be related to its surface features, as already suggested in general terms by Barthès & Luri (1999), Gray (2000), Platais et al. (2003), Svensson & Ludwig (2005), Bastian & Hefele (2005), Ludwig (2006), Eriksson & Lindegren (2007)?

The bottom panel of Fig. 15 shows the along-scan residuals $\Delta\eta$ for Betelgeuse against time (and Fig. 16 does the same for Antares and Rasalgethi), compared with the photocentre displacements P_x and P_y determined from the 3D simulation of Sect. 3.1.

From this comparison, we conclude that the photocentric noise, as predicted by The 3D simulations, does account for a substantial part of the "cosmic noise", but not for all of it. A possibility to reconcile predictions and observations could come from an increase of Betelgeuse's parallax (because the observed photocentric motion would then be larger for the σ_{P_θ} value fixed by the models), but this suggestion is not borne out by the recent attempt to improve upon Betelgeuse's parallax in the recent literature (Harper et al. 2008) (solution #2 in Table 2), by combining the Hipparcos astrometric data with VLA positions, as this new value is *lower* than both the original Hipparcos and van Leeuwen's values. The remaining possibility is that the 3D model discussed in Sect. 3.1 underestimates the photocentric motion. Indeed, Paper II showed that the RHD simulation fails to reproduce the TiO molecular band strengths in the optical region (see spectrum in Fig. 1). This is because the RHD simulations are constrained by execution time and therefore use a grey approximation for the radiative transfer. This is well justified in the stellar interior, but is a crude approximation in the optically thin layers. As a consequence, the thermal gradient is too shallow and weakens the contrast between strong and weak lines (Chiavassa et al. 2006). The resulting intensity maps look sharper than observations (see Paper II) and thus also the photocentre displacement should be affected. As described in Paper II, a new generation of non-grey opacities (five wavelength bins employed to describe the wavelength dependence of radiation fields) simulation is under development. This will change the mean temperature structure and the temperature fluctuations, especially in the outer layers where TiO absorption occurs.

6. Application to Gaia

6.1. Number of supergiant stars with detectable photocentric motion

In this section, we will use Eq. (16) to estimate the number of supergiants that will have a poor goodness-of-fit as a consequence of their photocentric motion. This equation requires knowledge of σ_{P_θ}, which will be kept as a free parameter in this section. In Sect. 3.1, $\sigma_{P_\theta} = 0.08$ AU was considered as typical for Betelgeuse-like supergiants, but Sect. 5 has provided hints that 3D models with grey opacities could somewhat underestimate this quantity. Moreover, according to Freytag (2001) and Ludwig (2006), σ_{P_θ} is expected to vary with the star's atmospheric pressure scale height, which in turn depends upon the star's absolute magnitude M_G. To explore the parameter space, we therefore need to know how σ_{P_θ} varies with M_G. This is especially important since on top of the condition in Eq. (16) relating d to $\sigma_{P_\theta}(M_G)$, there is another constraint coming from the requirement not to saturate the CCD, namely the Gaia magnitude G should be fainter than 5.6. All these constraints may be conveniently encapsulated in boundaries in the $d - M_G$ plane, as displayed in Fig. 19.

But first, we have to clarify the relation between σ_{P_θ} and M_G, which appears to be a critical ingredient in the present discussion. Unfortunately, 3D hydrodynamical models in the literature are scarce. Their main properties are collected in Table 3. These simulations are of two kinds: (i) *box-in-a-star* models cover only a small section of the surface layers of the deep convection zone, and the numerical box includes some fixed number of convective cells, which are large enough to not constrain the cells by the horizontal (cyclic) boundaries; (ii) *star-in-a-box* models, like the one described in this paper (Sect. 2), cover the whole convective envelope of the star and have been used to model RSG and AGB stars so far (see Freytag & Höfner 2008, for an AGB model), whereas the former simulations cover a large number of stellar parameters from white dwarf to red giant stars. The transition where the box-in-a-star models become inadequate occurs around $\log g \sim 1$, when the influence of sphericity becomes important; the star-in-a-box global models are then needed, but those are highly computer-time demanding and difficult to run, which is the reason why there are only very few models available so far.

Ludwig (2006) found that there is a tight correlation between the amplitude of the photocentric motion and the size of the granular cells. This size is related to the pressure scale height at optical-depth unity (Freytag 2001). The pressure scale height is defined as

$$\mathcal{H}_\mathrm{p} = \frac{k_B T_\mathrm{eff}}{mg}, \tag{17}$$

where g is the surface gravity, k_B is the Boltzmann constant and m is the mean molecular mass ($m = 1.31 \times m_\mathrm{H} = 1.31 \times 1.67 \times 10^{-24}$ g, for temperatures lower than 10 000 K). In the above expression, $\mathcal{H}_\mathrm{p}$ has the dimension of length. But in the remainder of this paper, we adopt instead the simplified definition

$$H_\mathrm{p} = \frac{T_\mathrm{eff}}{g}. \tag{18}$$

The law relating the standard deviation of the photocentre displacement to H_p may be inferred from Fig. 17, which displays the values from Table 3. The transition from the most evolved box-in-a-star model (with $\log H_\mathrm{p} \sim 2.57$) to our star-in-a-box model ($\log H_\mathrm{p} \sim 3.85$) is still unexplored; consequently, there

Table 3. Photocentre motion from 3D simulations.

Model	Configuration	$\log H_p$ (s^2 K/cm)	$\log \mathcal{H}_p$ (10^7 cm)	$\log(\sigma_{P_\theta})$ (AU)	$T_{\rm eff}$ (K)	$\log g$	R ($R_\odot$)	$M_{\rm bol}$
White dwarf[a]	box-in-a-star	–3.92	–3.15	–10.28	12000	8.00	1.28×10^{-2}	11.03
Sun[a]	box-in-a-star	–0.68	0.12	–7.12	5780	4.44	1	4.74
Procyon A[a]	box-in-a-star	–0.19	0.61	–6.37	6540	4.00	2.10	2.59
ξ Hydrae[a]	box-in-a-star	0.75	1.55	–5.45	4880	2.94	10.55	0.36
Cepheid[a]	box-in-a-star	1.66	2.46	–4.25	4560	2.00	30.17	–1.63
Red giant[a]	box-in-a-star	2.57	3.36	–3.02	3680	1.00	95.25	–3.19
RSG[b]	star-in-a-box	3.88	4.68	–1.10	3490	–0.34	832	–7.66

Notes. H_p is given with two different dimensions. [(a)] Svensson & Ludwig (2005). [(b)] This work, Sect. 3.1.

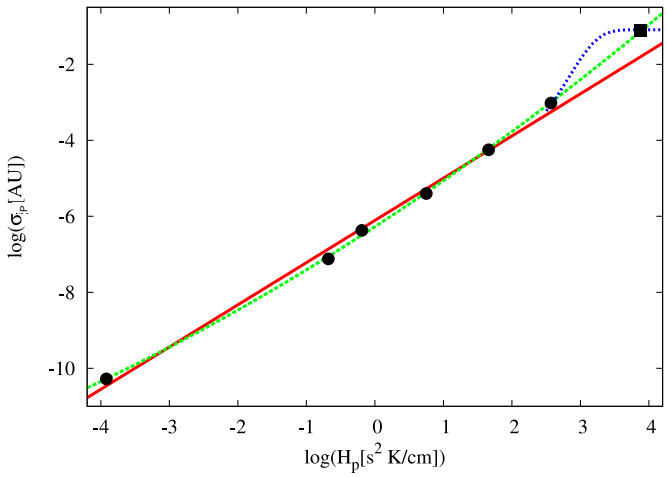

Fig. 17. Fits to the standard deviation σ_{P_θ} of the photocentric motion predicted from 3D simulations, as listed in Table 3, against the pressure scale height H_p. The equation of the (red) solid line is $\log \sigma_{P_\theta} = -6.110 + 1.110 \log(H_p)$ with $\chi^2 = 0.17$: the fit considers only the box-in-a-star models (filled circles) of Svensson & Ludwig (2005). The (green) dashed line (with equation $\log \sigma_{P_\theta} = -6.275 + 1.174 \log H_p + 0.039(\log H_p)^2$) is a fit to *all* the models of Table 3 (i.e., box-in-a-star models and star-in-a-box, the latter being represented by a filled square). The (blue) dotted line is an arbitrary exponential law that connects the last two points with the following equation $\log \sigma_{P_\theta} = -1.09 - 3.434 \exp(-0.00149 H_p)$.

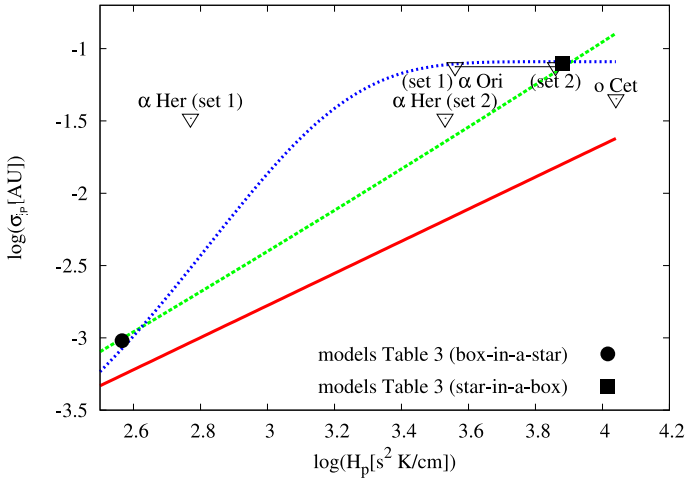

Fig. 18. Photocentre motions determined from interferometric observations for some evolved stars (see Table 4) overplotted on the different fits of the standard deviation σ_{P_θ} of the photocentric motion as a function of the pressure scale height H_p. The large open inverted triangles correspond to the standard deviations of the photocentre deviations for a given observed star. Star-in-a-box and box-in-a-star models correspond to the large filled square and circle respectively.

is no guarantee that the trend obtained at $\log H_p < 2.57$ may be extrapolated to higher H_p values. Different trends are therefore considered in Fig. 17 with a zoom in Fig. 18. The linear fit of $\log \sigma_{P_\theta}$ as a function of $\log H_p$ considers only the box-in-a-star models of Svensson & Ludwig (2005); the parabolic function is the best fit to all the models (including the star-in-a-box supergiant model). However, there is strong evidence in the simulations that the convective pattern changes significantly from the giant (big black circle symbol in Fig. 18) to the RSG simulations (big black squared symbol). The convective related surface structures grow enormously in the RSGs and together with the low effective temperature (i.e., the molecular absorption, strongly related to the temperature inhomogenities, is more important) increase the displacement of the photocentre position (i.e., σ_{P_θ} is larger). Thus, the parabolic fit, which considers all the simulations' configurations together, is not a completely correct approach because of the physical changes reported above. Since the transition region between the box-in-a-star (giant stars) and star-in-a-box models (RSG stars) is still unexplored, we consider an extreme transition by adopting an arbitrary exponential law to relate the last two model simulation points (i.e., the transition region between the box-in-a-star and star-in-a-box models). Paper I pointed out that the reasons for the peculiar convective pattern in RSGs could be (i) in RSGs, most of the downdrafts will not grow fast enough to reach any significant depth before they are swept into the existing deep and strong downdrafts enhancing the strength of neighbouring downdrafts; (ii) radiative effects and smoothing of small fluctuations could matter; (iii) sphericity effects and/or numerical resolution (or lack of it).

To see which among these three possible trends has to be preferred, we made a compilation of photocentric displacements P from interferometric observations of various supergiants available in the literature (see Fig. 18). Supergiants and Miras have been observed several times in the last decade with interferometers, often revealing the presence of surface brightness asymmetries. In several cases (α Ori, α Her, and o Cet; see Table 4 for the data list and references; more stars will be presented in Sacuto et al., in preparation), the observations could be represented by parametric models consisting of a uniform disc plus one (or more) bright or dark spots. Using the parameters of the spots fitting the interferometric data, we computed the positions of the

Table 4. References used to compute the photocentric shifts from interferometric data.

Name	$\log g$	$T_{\rm eff}$ (K)	$\log H_{\rm p}$ $\log$ (s^2 K/cm)	ϖ (mas)	P (mas)	P (AU)	λ (nm)	Date	References
α Ori	−0.3	3650	3.86	6.56					Harper et al. (2008) (set 1)
	0.0	3650	3.56	6.56					Levesque et al. (2005) (set 2)
					1.216	0.185	700	02/1989	Buscher et al. (1990), Wilson et al. (1992, 1997), Tuthill et al. (1997), Young et al. (2000), Tatebe et al. (2007), Haubois et al. (2009)
					1.637	0.249	710	01/1991	
					0.369	0.056	700	01/1992	
					0.694	0.106	700	01/1993	
					0.550	0.084	700	09/1993	
					0.427	0.065	700	12/1993	
					0.144	0.022	700	11/1994	
					0.395	0.060	700	12/1994	
					0.302	0.046	700	12/1994	
					0.142	0.021	700	01/1995	
					0.025	0.004	700	01/1995	
					0.009	0.001	700	11/1997	
					$\langle P \rangle$	0.075			
					$\langle P^2 \rangle$	0.011			
					σ_P	0.075			
α Her	0.76	3400	2.77	9.07					El Eid (1994) (set 1)
	0.0	3450	3.53	9.07					Levesque et al. (2005) (set 2)
					0.340	0.037	710	07/1992	Tuthill et al. (1997)
					0.765	0.084	710	06/1993	
					$\langle P \rangle$	0.060			
					$\langle P^2 \rangle$	0.004			
					σ_P	0.033			
o Cet	–0.6	2900	4.06	10.91					Tuthill et al. (1999)
					1.202	0.110	710	07/1992	
					0.850	0.078	700	01/1993	
					0.990	0.091	710	09/1993	
					1.950	0.179	710	12/1993	
					$\langle P \rangle$	0.114			
					$\langle P^2 \rangle$	0.015			
					σ_P	0.045			

Notes. Stellar parameters are from Levesque et al. (2005) and Harper et al. (2008) for α Ori and α Her (set 2), El Eid (1994) for α Her (set 1) and Fernie (1995) for o Cet. Parallaxes are from van Leeuwen (2007b). Only observations in the optical range were kept.

photocentre for all observations of a given star and from there the standard deviation of these photocentric positions, which was then plotted against $H_{\rm p}$ in Fig. 18. These observational data suggest that the exponential and quadratic fits of the simulation data are to be preferred over the linear extrapolation of the box-in-a-star values (Fig. 18). We stress, however, that the surface gravity for supergiants like α Her and α Ori are quite uncertain (see Table 4) and also the highly uncertain metallicity differences might play a role here.

The number of stars with photocentric motions detectable by Gaia as having bad fits (i.e., high goodness-of-fit $F2$ values) may now be estimated as follows. The Besançon Galaxy model (Robin et al. 2004) was used to generate a sample of bright giants and supergiants ($M_V < 0$) in the region $0 \leq l \leq 180$ and $-20 \leq b \leq 20$ of our Galaxy (where l and b are the galactic coordinates). The reddening was added separately using the extinction model from Drimmel et al. (2003). For each one of the the 361 069 stars in that sample, we assign the corresponding expected standard deviation of the photocentre displacement σ_{P_θ} taken from the exponential or parabolic laws of Fig. 17 (each of these two possibilities was tested separately), with $H_{\rm P}$ estimated from Eq. (18)[7].

[7] We note in passing that in the Besançon sample there is no star matching Betelgeuse parameters if one adopts $\log g = -0.3$ for its surface gravity, yielding $\log H_{\rm p} = 3.85$. If on the other hand, one adopts $\log g = 0.0$, we get $\log H_{\rm p} = 3.55$ and Betelgeuse is then matched by stars from the Besançon sample. This can be seen from the lower panel of Fig. 20, since Betelgeuse has $M_G = -6.4$, when adopting

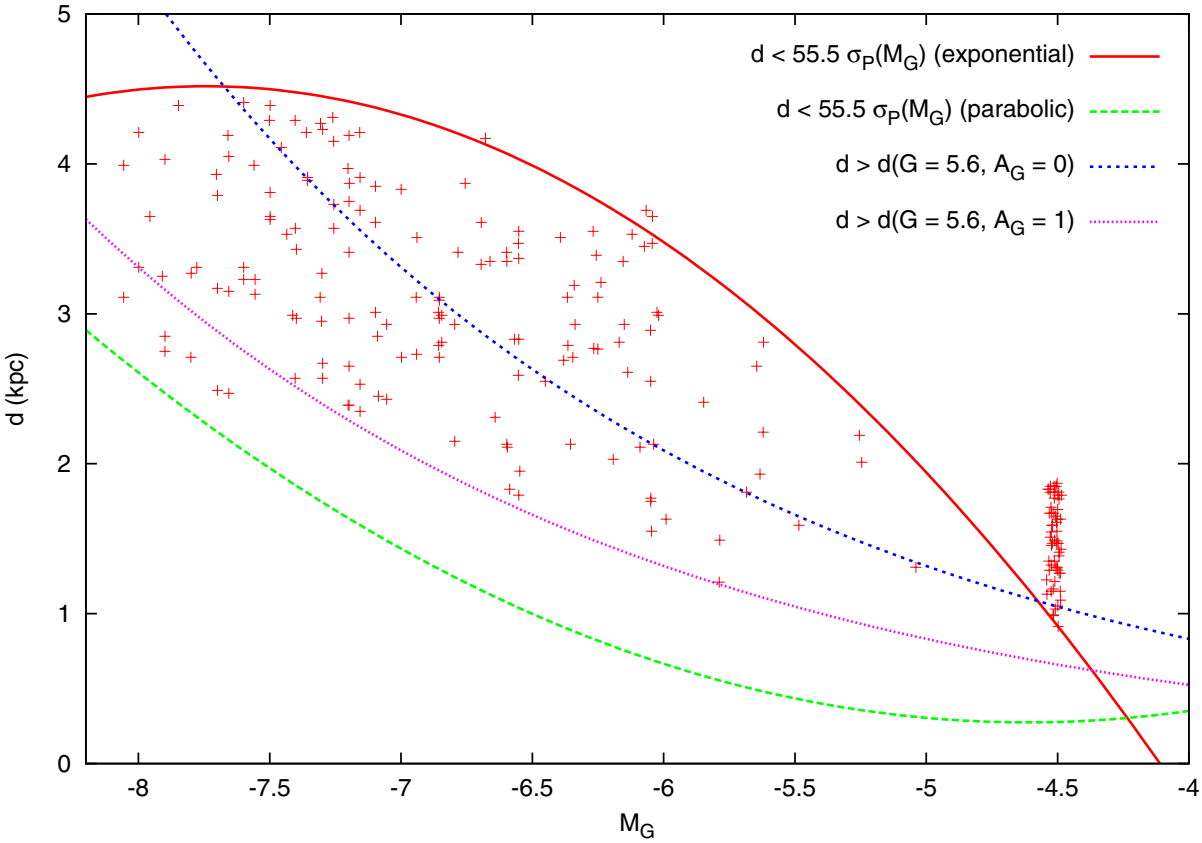

Fig. 19. Location in the (M_G, d) plane for supergiants with a photocentre noise (of standard deviation σ_{P_θ}) significantly altering the goodness-of-fit of the astrometric solution (see text), for the case of an exponential link between box-in-a-star and star-in-a-box models (see Fig. 18 and text).

We then computed the number of stars that fulfill the condition expressed by Eq. (16), and have at the same time $G > 5.6$ in order not to saturate the Gaia CCD detectors. The conversion between V and G magnitudes has been done from the colour equation (adopted from the *Gaia Science Performance* document[8,9]):

$$G = V - 0.0107 - 0.0879\,(V-I) - 0.1630\,(V-I)^2 + 0.0086\,(V-I)^3. \quad (19)$$

With the exponential law, we found 215 supergiants (among the 361 069 of the full sample, representing half the galactic plane) fulfilling these two conditions. They are displayed in Fig. 19 in the $d - M_G$ plane, and are basically confined to a crescent delineated by the conditions $G > 5.6$ (corresponding to the two lines with an upwards concavity, labelled $G > 5.6$; the two lines correspond to two values of the extinction in the G band: $A_G = 0$ and 1) and $d \leq 55.5\ \sigma_{P_\theta}(M_G)$ (Eq. (16), corresponding to the green dashed line with a downwards concavity). The latter line is based on a fiducial relationship between σ_{P_θ} and M_G, as shown in Fig. 20. Some supergiants nevertheless fall outside the crescent defined above, simply because of the scatter affecting the $\sigma_{P_\theta} - M_G$ relationship (Fig. 20). Obviously, all supergiants of interest are bright in the G band, in the range 5.6 to about 8 and will thus be easily identifiable during Gaia data processing.

With the parabolic law, only one supergiant matches the conditions: it is the brightest supergiant located in the upper left corner of Fig. 20 (green point in the lower panel; note that in Fig. 19 this star is not located below the parabolic threshold line as expected, because that line is based on a mean $\sigma_P - M_G$ relation – see Fig. 20 –, and that supergiant happens to have a σ_P value much above average, as seen in Fig. 20). Thus, Fig. 19 suggests that the "parabolic" link between box-in-a-star and star-in-a-box models of Fig. 17 and 18 is a limiting case: for photocentric motions to be detected by Gaia, the σ_{P_θ} vs M_G relation has to lie above this limiting case (depicted as the green solid line in Fig. 18).

In Fig. 19 there is a cluster of stars at $M_G = -4.5$ (corresponding to $\log T_{\rm eff} \sim 3.5$ and $\log g \sim 0.4$), which corresponds to bright giants or asymptotic giant branch (AGB) stars. They are also clearly seen in Fig. 20 as the cluster at $\sigma_{P_\theta} = 0.035$ AU (with the exponential law) or 0.01 AU (with the parabolic law). Because these stars belong to a population different from supergiants (with masses of the order 1 $M_\odot$), they are not necessarily confined to the galactic plane as supergiants are. Hence another sample, now covering a quarter of the sky ($0° \leq l \leq 180°$, $b \geq 0°$), was generated from the Besançon model and contains 702 211 giants and bright giants. In this sample, 938 stars satisfy the condition of detection of the photocentric motion with the exponential law, and none with the parabolic law. The relation $M_G - \sigma_{P_\theta}$ thus appears as an essential ingredient, but unfortunately quite uncertain still, especially for those among the bright giants that are pulsating as long-period variables. The pulsation

$M_{\rm bol} = -7.5$ from the apparent bolometric flux 111.67×10^{-13} W cm^{-2} (Perrin et al. 2004) and the parallax 6.56 mas (van Leeuwen 2007a), $V-G = 0.98$ from $V-I = 2.32$ (ESA 1997) and Eq. (19), $BC_V = -2.05$ from the apparent bolometric flux and $V = 0.42$ (Johnson et al. 1966).

[8] http://www.rssd.esa.int/index.php?project=GAIA&page=Science_Performance

[9] http://www.rssd.esa.int/SYS/docs/ll_transfers/project=PUBDB&id=448635.pdf

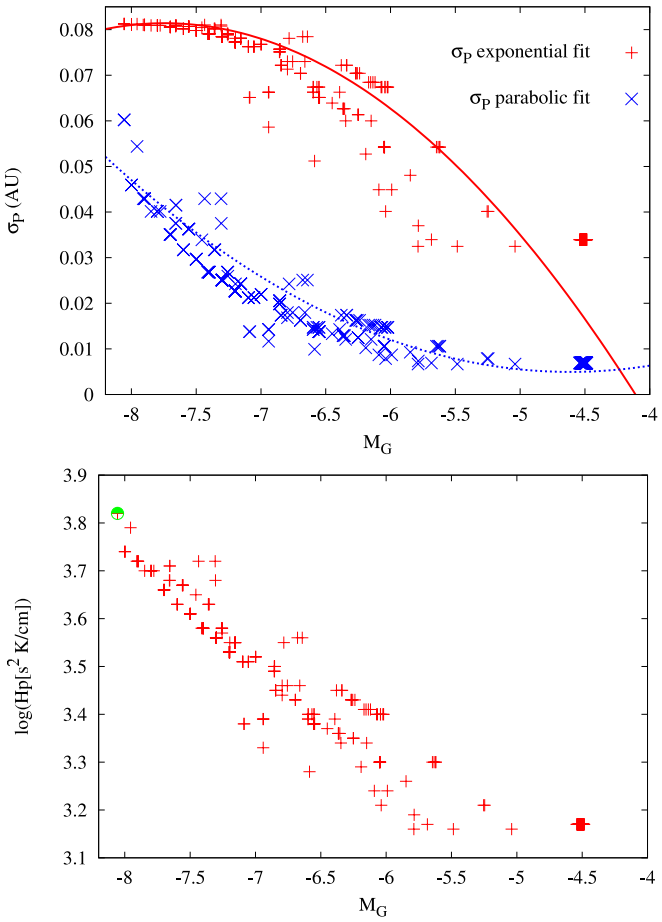

Fig. 20. *Upper panel*: the relation between σ_{P_θ} and M_G for supergiants and bright giants, assuming either an exponential (red plusses) or a parabola (blue crosses) to connect the box-in-a-star with the star-in-a-box models (Fig. 18). The equation of the dashed green line (through the red plusses) is $\sigma_{P_\theta} = -0.29 - 0.10\ M_G - 0.0062\ M_G^2$, whereas the equation of the magenta dotted line (through the blue crosses) is $\sigma_{P_\theta} = 0.083 + 0.034\ M_G + 0.0037\ M_G^2$. *Lower panel*: same as the upper panel, for the relation between the pressure scale height Hp and the absolute magnitude in the Gaia G band. Only stars with a detectable photocentric motion (for the exponential fit: red crosses; for the parabolic fit: green dot) have been plotted.

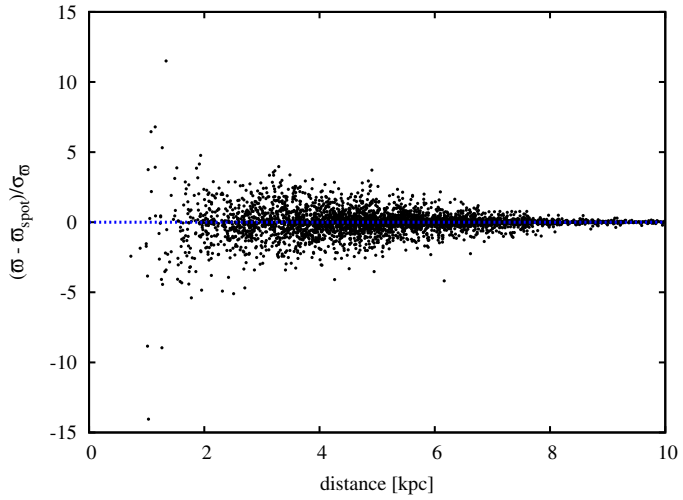

Fig. 21. Comparison of parallaxes for supergiant stars with and without surface brightness asymmetries (spots), normalised to σ_ϖ. The stars falling on the horizontal line with ordinate 0 are very reddened stars, are consequently quite faint, and therefore have large errors on their astrometric measurements and thus on their parallax.

makes the modelling especially difficult (see for instance Freytag & Höfner 2008; Chiavassa et al. 2010b, for an application of 3D AGB models to the star VX Sgr). Nevertheless, numerous observations have revealed their surface brightness asymmetries (e.g., Ragland et al. 2006, and references therein).

6.2. Impact on the parallaxes

To evaluate the impact of the photocentric shift on the parallax, we proceeded as follows. The sampling times, scanning angles, along-scan measurements and their errors were obtained from the Gaia Object Generator v7.0 (GOG[10], Isasi et al. 2010) for the supergiant stars from the sample generated using the Besançon model described in the previous section. A photocentric motion deduced from the photocentre position computed from the snapshots of the red supergiant model (see Fig. 3) was added on the along-scan measurements (the photocentric shift was converted from linear to angular shifts, according to the known stellar distance). The red supergiant model gives a single photocentre position sequence. Yet the sequence for every star should be different. Therefore the sequence was rotated for every star by a random angle before being added to the along scan measurements. The astrometric parameters were then retrieved by solving the least-squares equation (Eq. (7)), separately with and without surface brightness asymmetries. The resulting parallaxes are compared in Fig. 21.

Figure 23 presents the histogram of the quantity $(\varpi - \varpi_{\rm spot})/\sigma_\varpi$ for three different ranges of distances. Obviously the distribution, which is quite peaked at zero for distant stars, becomes wider for nearer stars, meaning that the ratio of the error on the parallax to its formal error increases with decreasing distance. Similarly, the fits of the astrometric data are worse for stars closer by, and this effect is clearly seen in Fig. 24, displaying the relation between the goodness-of-fit parameter $F2$ and the distance. The run of $F2$ with distance is consistent with that predicted by Eq. (12), for $\nu = 70$, $\sigma_{P_\theta} = 0.1$ AU and $\sigma_\eta = 0.03$ mas.

Coming back to Fig. 22, it is remarkable that the relative error on the parallax, namely $(\varpi - \varpi_{\rm spot})/\varpi$ is almost independent of the distance and amounts to a few percents. This is in deed easy to understand if one assumes that the difference $\varpi - \varpi_{\rm spot}$ must somehow be proportional to the amplitude of the excursion of the photocentre on the sky, which must in turn be related to θ, the angular radius of the star on the sky; therefore, $(\varpi - \varpi_{\rm spot})/\varpi = \alpha\theta/\varpi = \alpha R$, where α is the proportionality constant and R is the linear radius of the star (expressed in AU). Thus we conclude that the relative error on the parallax is independent of the distance, and is simply related to the excursion of the photocentre expressed in AU.

These simulations for a sample of Betelgeuse-like supergiants therefore allow us to confirm the results obtained in Sect. 6.1 (and Fig. 19), in particular that the impact on the goodness-of-fit remains noticeable up to about 5 or 6 kpc (Fig. 24).

[10] http://gaia-gog.cnes.fr

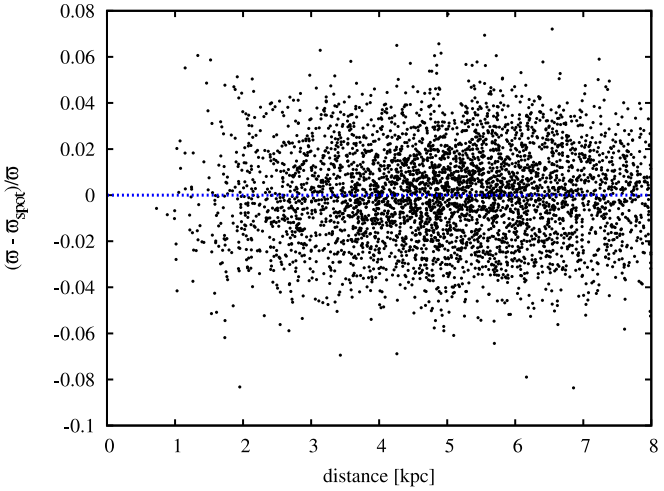

Fig. 22. Same as Fig. 21, but normalised by the parallax. Note how the relative parallax error is almost independent of the distance.

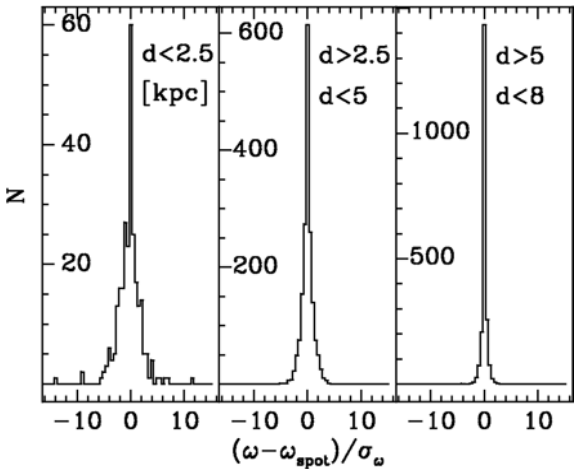

Fig. 23. Histograms of the relative error on the parallax of supergiant stars, for different ranges of distances.

7. Conclusion

We provided astrometric and photometric predictions from 3D simulations of RSGs to evaluate the impact of the surface brightness variations on the astrometric parameters of these stars to be derived by Gaia.

We found that the global-scale convective pattern of RSGs cause strong variability in the position of the photocentre, P. From a 3D simulation of a Betelgeuse-like supergiant, $\langle P \rangle = 0.132 \pm 0.065$ AU (i.e., more than 3% of the stellar radius) showing excursions from 0.005 to 0.3 AU over the five years of simulation. In addition, the spectra show large fluctuations in the red and blue Gaia bands of up to 0.28 mag in the blue and 0.15 mag in the red. The Gaia colour index (blue – red) also fluctuates strongly with respect to time. Therefore, the uncertainties on [Fe/H], $T_{\rm eff}$ and $\log g$ should be revised upwards for RSGs because of their convective motions. We furthermore provided predictions for interferometric observables in the Gaia filters that can be tested against observations with interferometers such as VEGA at CHARA.

Then we studied the impact of the photocentric noise on the astrometric parameters. For this purpose, we considered the standard deviation of the photocentre displacement predicted

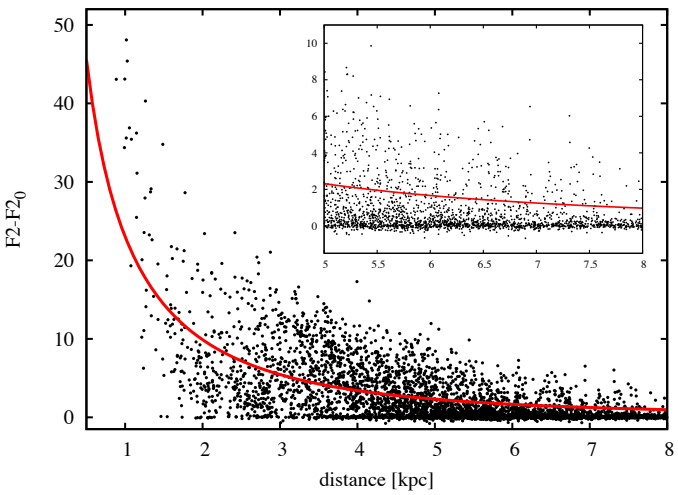

Fig. 24. Same as Fig. 21 for the goodness-of-fit $F2$. The solid line corresponds to the prediction from Eq. (12), with $\nu = 70$, $\sigma_{P_\theta} = 0.1$ AU and $\sigma_\eta = 0.03$ mas. Part of the large scatter at intermediate distances (2 to 4 kpc) is caused by a different CCD gating sequence (see de Bruijne 2005; Lindegren 2010).

by the RHD simulation, sampled as Gaia will do (both timewise and directionwise). We called this quantity σ_{P_θ}, where θ is the position angle of the scanning direction on the sky, and we found $\sigma_{P_\theta} = 0.08$ AU for Betelgeuse-like supergiants. This photocentric noise can be combined with $\sigma_\eta = 30\ \mu$as (the error on the along-scan position η) for Gaia to determine the maximum distance ($d < 4.4$ kpc) up to which a photocentric motion with $\sigma_{P_\theta} = 0.08$ AU will generate an astrometric noise of the order of the astrometric error on one measurement (more precisely 0.6 times that error, yielding an increase of the $F2$ goodness-of-fit parameter by two units). The value $\sigma_{P_\theta} = 0.08$ AU could even be somewhat underestimated, as we guessed from the comparison of the along-scan Hipparcos residuals for Betelgeuse with the RHD predictions. We concluded that the predicted photocentric noise does account for a substantial part of the Hipparcos "cosmic noise" for Betelgeuse and Antares, but not for all of it. This may be because the temperature stratification in the RHD models is not completely correct owing to the grey approximation used for the radiative transfer. The resulting intensity maps have higher contrast than the observations, as shown in Paper II, and the photocentre position can therefore be affected as well. New simulations with wavelength resolution (i.e., non-grey opacities) are in progress and they will be tested against these observations.

We estimated how many RSGs might have an abnormally large goodness-of-fit parameter $F2$. We found that the photocentric noise should be detected by Gaia for a number of bright giants and supergiants varying between 2 and about 4190 (215 supergiants in each half of the celestial sphere and 940 bright giants in each quarter of the sphere; see Sect. 6.1), depending upon the run of σ_{P_θ} with the atmospheric pressure scale height $H_{\rm P}$, and to a lesser extent, depending on galactic extinction. The theoretical predictions of 3D simulations presented in this work will be tested against the multi-epoch interferometric observations of a sample of giants and supergiants (Sacuto et al., in prep.), with the hope to better constrain this $\sigma_{P_\theta} - H_{\rm P}$ relation. In a forthcoming paper (Pasquato et al., in prep.), we will evaluate how the Gaia reduction pipeline behaves when facing the bright-giants and supergiants granulation. More specifically, we will show that the

distance to the star is the main driver fixing which one among all the possible solution types (single-star, acceleration, orbital, stochastic) is actually delivered by the pipeline (the acceleration and orbital solutions being obviously spurious).

Finally, a very important conclusion is that the parallax for Betelgeuse-like supergiants may be affected by an error of a few percents. For the closest supergiants ($d < 2.5$ kpc), this error may be up to 15 times the formal error σ_{ϖ} (see Fig. 21) resulting from the measurement errors and estimated from the covariance matrix. In a forthcoming paper (Pasquato et al., in prep.), we will moreover show that this error is sensitive to the time scale of the photocentric motion (which is in turn fixed by the granulation and the stellar rotation).

There is little hope to be able to correct the Gaia parallaxes of RSGs from this parallax error, without knowing the run of the photocentric shift for each considered star. Nevertheless, it might be of interest to monitor the photocentric deviations for a few well selected RSGs during the Gaia mission. Ideally, this would require imaging the stellar surface, although monitoring of the phase closure on three different base lines may already provide valuable information on the size of the inhomogeneities present on the stellar surface (see Sacuto et al., in prep.). The best-suited targets for that purpose would be supergiants with G magnitudes just above the Gaia saturation limit of 5.6, where the astrometric impact is going to be maximum, and at the same time, still within reach of the interferometers. The corresponding diameter will be of the order of 4 mas (derived from the radius 830 $R_{\odot}$ for a Betelgeuse-like supergiant seen at a distance of 2 kpc if $G = 5.6$, $A_G = 1$, and $M_G = -6.6$). A search for G, K, or M supergiants (of luminosity classes I, Ia, Iab, or Ib) with $5.6 \leq V \leq 8$ in the SIMBAD database yielded only three stars (XX Per, HD 17306, and WY Gem) matching these criteria, the latter being a spectroscopic binary, which will disturb the radius measurement and is thus unsuited for this purpose. It may therefore be necessary to select these targets from the Gaia data themselves, after the first year of the mission.

Acknowledgements. E.P. is supported by the ELSA (European Leadership in Space Astrometry) Research Training Network of the FP6 Programme. S.S. acknowledges funding by the Austrian Science Fund FWF under the project P19503-N13. We thank the CINES for providing some of the computational resources necessary for this work. We thank DPAC-CU2, and especially X. Luri and Y. Isasi, for help with the use of GOG. A.C. thanks G. Jasniewicz for enlightening discussions. B.F. acknowledges financial support from the *Agence Nationale de la Recherche* (ANR), the *"Programme National de Physique Stellaire"* (PNPS) of CNRS/INSU, and the *"École Normale Supérieure"* (ENS) of Lyon, France, and from the *Istituto Nazionale di Astrofisica/Osservatorio Astronomico di Capodimonte* (INAF/OAC) in Naples, Italy.

Appendix A: Formal errors on the parameters of a least-squares minimisation

We provide here a short demonstration of a well-known statistical result (see e.g., Press et al. 1992), which may appear counter-intuitive in the present context, namely that the presence of an extra-source of unmodelled noise will not change the formal errors on the parameters derived from a least-squares minimisation.

Consider the case where the data points (x_i, y_i) $(i = 1, ..., N)$ must be fitted by a general linear model

$$y(x) = \Sigma_{k=1}^{M} a_k \, X_k(x), \tag{A.1}$$

where $X_k(x)$ $(k = 1, ..., M)$ are M arbitrary (but known) functions of x, which may be wildly non-linear. The merit function is defined as

$$\chi^2 = \sum_{i=1}^{N} \left[\frac{y_i - \Sigma_{k=1}^{M} a_k \, X_k(x_i)}{\sigma_i} \right]^2, \tag{A.2}$$

where σ_i is the measurement error on y_i presumed to be known. To simplify the notation, we define the *design matrix* $\mathbf{A}$ (of size $N \times M$) by

$$A_{ij} = \frac{X_j(x_i)}{\sigma_i}, \tag{A.3}$$

the vector $\boldsymbol{b}$ of (normalised) measured values, of length N:

$$b_i = \frac{y_i}{\sigma_i}, \tag{A.4}$$

and finally the vector $\boldsymbol{a}$ of length M whose components are the parameters a_k $(k = 1, ..., M)$ to be fitted. The least-squares problem may thus be rephrased as

$$\text{find } \boldsymbol{a} \text{ that minimises } \chi^2 = |\mathbf{A}\boldsymbol{a} - \boldsymbol{b}|^2,$$

whose solution may be written

$$\left(\mathbf{A}^{\mathrm{T}}\mathbf{A}\right)\boldsymbol{a} = \mathbf{A}^{T}\boldsymbol{b}, \tag{A.5}$$

with $\mathbf{C} \equiv \left(\mathbf{A}^{T}\mathbf{A}\right)^{-1}$ being the variance-covariance matrix describing the uncertainties[11] of the estimated parameters $\boldsymbol{a}$. The crucial point to note here is that matrix $\mathbf{C}$ involves the measurement uncertainties σ_i but not the measurements y_i themselves. Therefore, changing y_i, in the presence of an unmodelled process (like photocentric motion) without changing the measurement uncertainties σ_i, will not change the formal errors on the resulting parameters $\boldsymbol{a}$. But of course, χ^2 along with the goodness-of-fit parameter $F2$ (see Eq. (10)) will be larger if there is of a photocentric noise, as the scatter around the best astrometric solution will be larger than expected solely from the measurement errors. Therefore, it is $F2$ and its associated χ^2, but not the formal parallax error, which bear the signature of the presence of photometric noise.

References

Asplund, M., Grevesse, N., & Sauval, A. J. 2006, Communi. Asteroseismol., 147, 76
Bailer-Jones, C. A. L. 2010, MNRAS, 403, 96
Barthès, D., & Luri, X. 1999, Baltic Astron., 8, 285
Bastian, U., & Hefele, H. 2005, in The Three-Dimensional Universe with Gaia, ed. C. Turon, K. S. O'Flaherty, & M. A. C. Perryman, ESA SP, 576, 215
Berger et al.(2010), A&ARv, submitted
Buscher, D. F., Baldwin, J. E., Warner, P. J., & Haniff, C. A. 1990, MNRAS, 245, 7P
Chiavassa, A., Plez, B., Josselin, E., & Freytag, B. 2006, in SF2A-2006: Semaine de l'Astrophysique Francaise, ed. D. Barret, F. Casoli, G. Lagache, A. Lecavelier, & L. Pagani , 455
Chiavassa, A., Plez, B., Josselin, E., & Freytag, B. 2009, A&A, 506, 1351
Chiavassa, A., Haubois, X., Young, J. S., et al. 2010a, A&A, 515, A12
Chiavassa, A., Lacour, S., Millour, F., et al. 2010b, A&A, 511, A51
de Bruijne, J. H. J. 2005, in The Three-Dimensional Universe with Gaia, ed. C. Turon, K. S. O'Flaherty, & M. A. C. Perryman, ESA SP, 576, 35
Drimmel, R., Cabrera-Lavers, A., & López-Corredoira, M. 2003, A&A, 409, 205
El Eid, M. F. 1994, A&A, 285, 915
Eriksson, U., & Lindegren, L. 2007, A&A, 476, 1389

[11] In deed, this statement only holds if the errors σ_i are normally distributed, which is supposed to be the case for the specific problem under consideration (namely, the Gaia along-scan measurement errors).

ESA. 1997, The Hipparcos and Tycho Catalogues (ESA SP-1200)
Fernie, J. D. 1995, AJ, 110, 2361
Freytag, B. 2001, in 11th Cambridge Workshop on Cool Stars, Stellar Systems and the Sun, ed. R. J. Garcia Lopez, R. Rebolo, & M. R. Zapaterio Osorio, ASP Conf. Ser., 223, 785
Freytag, B., & Höfner, S. 2008, A&A, 483, 571
Freytag, B., Steffen, M., & Dorch, B. 2002, Astron Nachr., 323, 213
Gray, D. F. 2000, ApJ, 532, 487
Gustafsson, B., Edvardsson, B., Eriksson, K., et al. 2008, A&A, 486, 951
Harper, G. M., Brown, A., & Guinan, E. F. 2008, AJ, 135, 1430
Haubois, X., Perrin, G., Lacour, S., et al. 2009, A&A, 508, 923
Isasi, Y., Figueras, F., Luri, X., & Robin, A. C. 2010, in Highlights of Spanish Astrophysics V, ed. J. M. Diego, L. J. Goicoechea, J. I. González-Serrano, & J. Gorgas (Berlin: Springer Verlag), 415
Johnson, H. L., Iriarte, B., Mitchell, R. I., & Wisniewski, W. Z. 1966, Communications of the Lunar and Planetary Laboratory, 4, 99
Jordi, C., & Carrasco, J. M. 2007, in The Future of Photometric, Spectrophotometric and Polarimetric Standardization, ed. C. Sterken, ASP Conf. Ser., 364, 215
Jordi, C., Gebran, M., Carrasco, J. M., et al. 2010, A&A, 523, A48
Levesque, E. M., Massey, P., Olsen, K. A. G., et al. 2005, ApJ, 628, 973
Lindegren, L. 2010, in Relativity in Fundamental Astronomy: Dynamics, Reference Frames, and Data Analysis, IAU Symp. 261, ed. S. A. Klioner, P. K. Seidelmann, & M. H. Soffel (Cambridge: Cambridge University Press), 261, 296
Lindegren, L., Babusiaux, C., Bailer-Jones, C., et al. 2008, in A Giant Step: from Milli- to Micro-arcsecond Astrometry, ed. W. J. Jin, I. Platais, & M. A. C. Perryman (Cambridge: Cambridge University Press), IAU Symp. 248, 217
Ludwig, H.-G. 2006, A&A, 445, 661
Luri, X., Babusiaux, C., & Masana, E. 2005, in The Three-Dimensional Universe with Gaia, ed. C. Turon, K. S. O'Flaherty, & M. A. C. Perryman, ESA SP, 576, 357
Mourard, D., Clausse, J. M., Marcotto, A., et al. 2009, A&A, 508, 1073
Perrin, G., Ridgway, S. T., Coudé du Foresto, V., et al. 2004, A&A, 418, 675
Perryman, M. A. C., de Boer, K. S., Gilmore, G., et al. 2001, A&A, 369, 339
Platais, I., Pourbaix, D., Jorissen, A., et al. 2003, A&A, 397, 997
Pourbaix, D., & Jorissen, A. 2000, A&AS, 145, 161
Press, W., Teutolsky, S., Vetterling, W., & Flannery, B. 1992
Ragland, S., Traub, W. A., Berger, J., et al. 2006, ApJ, 652, 650
Robin, A. C., Reylé, C., Derrière, S., & Picaud, S. 2004, A&A, 416, 157
Stuart, A., & Ord, J. K. 1994, Kendall's advanced theory of statistics. Vol. 1: Distribution theory, ed. A. Stuart, & J. K. Ord
Svensson, F., & Ludwig, H. 2005, in 13th Cambridge Workshop on Cool Stars, Stellar Systems and the Sun, ed. F. Favata, G. A. J. Hussain, & B. Battrick, ESA SP, 560, 979
Tatebe, K., Chandler, A. A., Wishnow, E. H., Hale, D. D. S., & Townes, C. H. 2007, ApJ, 670, L21
Thévenin, F. 2008, Phys. Scripta T, 133, 014010
Tuthill, P. G., Haniff, C. A., & Baldwin, J. E. 1997, MNRAS, 285, 529
Tuthill, P. G., Haniff, C. A., & Baldwin, J. E. 1999, MNRAS, 306, 353
van Leeuwen, F. 2007a, Hipparcos, the New Reduction of the Raw Data (Springer Verlag)
van Leeuwen, F. 2007b, A&A, 474, 653
van Leeuwen, F., & Evans, D. W. 1998, A&AS, 130, 157
Wilson, R. W., Baldwin, J. E., Buscher, D. F., & Warner, P. J. 1992, MNRAS, 257, 369
Wilson, R. W., Dhillon, V. S., & Haniff, C. A. 1997, MNRAS, 291, 819
Young, J. S., Baldwin, J. E., Boysen, R. C., et al. 2000, MNRAS, 315, 635